A semi implicit compressible solver for two-phase flows of real fluids

Annafederica Urbano, Marie Bibal, Sébastien Tanguy

A semi implicit compressible solver for two-phase flows of real fluids

A. Urbano [a,*], M. Bibal [b], S. Tanguy [c]

[a] ISAE SUPAERO, Université de Toulouse, Toulouse, France
[b] IMFT, Université de Toulouse, CNRS, INP, Toulouse, France
[c] IMFT, Université de Toulouse, CNRS, Université Toulouse 3 - Paul Sabatier, France

Keywords:
Compressible two-phase flows
Real fluids equations of state
Acoustics interface interactions
Ghost fluid method
Semi-implicit projection method
Free convection

A B S T R A C T

The development of numerical solvers able to simulate compressible two-phase flows is still a great challenge in computational fluid dynamics. The interaction between acoustic waves and interfaces is of major concern for several engineering and biomedical applications, among which atomization in combustion chambers, cavitation problems, underwater explosions and bubble shock interactions. For instance, there are experimental evidences that acoustic waves can have an important effect on the atomization process, and this could have a great impact on combustion. However, usual approaches for DNS of primary atomization are based on incompressible solvers and therefore are not able to capture the propagation of acoustic waves and therefore cannot be used to simulate such phenomena. The numerical problem associated with the simulation of compressible two-phase flows is challenging, mostly because of the huge spatial variations of the speed of sound and the corresponding low Mach number in the liquid phase. In the present work, a numerical solver able to study subsonic compressible two-phase flows is presented. The solver is based on a complete formulation of the Navier-Stokes equations with real fluid equations of state, which are solved with a semi-implicit projection method. It is shown that the solver can handle a large range of compressible subsonic flows, both for a single phase or for two phases, as the flow induced by free convection, a bubble expansion in isothermal or isentropic conditions, and interaction between acoustic waves and liquid-gas interfaces. Eventually, attention will be given to the simulation of a water droplet in air, under the excitation of a stationary acoustic wave. It is also shown that the solver exhibits equivalent performances as an incompressible solver in configurations where compressible effects have no effects.

1. Introduction

Numerical solvers for compressible flows, with an interface capturing or interface tracking approach, are mainly based on fully explicit shock-capturing methods, and have been developed in the framework of high Mach number flows, in particular for the study of the interaction between drops or bubbles and shock waves [17,53,9,19], or atomization with ultrasonics [44]. The major drawbacks of these explicit approaches are the stability condition associated with the acoustic propagation and

* Corresponding author.
E-mail address: annafederica.urbano@isae-supaero.fr (A. Urbano).

https://doi.org/10.1016/j.jcp.2022.111034

the loss of accuracy in the low Mach number regime which can be particularly stringent in the liquid phase (due to the high speed of sound). That makes these methodologies inefficient at low Mach numbers. To avoid the low Mach number constraint associated with the liquid phase, mixed approaches, considering a compressible gas and incompressible liquid, have been proposed (see for instance [7,8,1,26]). However, such approaches are limited to describe the interaction of a liquid with acoustic waves since they do not allow the acoustic waves propagation in the liquid phase.

In recent years another class of methods, based on a semi-implicit compressible projection approach, have been developed for two-phase flows [24,20,42,18], which are derived from the single-phase formulations proposed by [57] and by [27]. The main idea is to split the equations in an advection and an acoustic part. The advection part is solved with an explicit scheme while the acoustic part is solved with an implicit scheme with a projection method, thus removing the stringent time step constraint associated with the propagation of acoustic waves. The methodology is also suitable to treat low Mach number compressible flows since it is asymptotically preserving [24], that is the incompressible formulation is retrieved when the Mach number goes to zero. This class of algorithms differs from another class of pressure-based solvers, SIMPLE [39] and its variants (SIMPLEC, SIMPLER,...) [16,38], which require solving a nonlinear iterative system. Such algorithms are beneficial for the computation of steady-state flows, but their use may not be the most efficient numerical strategy for performing Direct Numerical Simulation of unsteady flows that require accurate time-scale solving.

The compressible projection method has attractive numerical properties for the simulation of two-phase flows at low Mach number. However, formulations of this algorithm are usually isentropic, and no viscous and heat conduction effects are taken into consideration, even though they are of great importance in most applications. Only a few number of works present a formulation for two-phase compressible flows including non-isentropic effects [24,30,10]. In particular Jemison et al. [24] presented an approach to include non-viscous terms, and later extended it to include heat conduction in [2]. Their solver is based on a conservative variables formulation, and viscous effects are considered in the total energy equation. However, while conserving the total energy, this approach fails in retrieving a pressure consistent with the equation of state at each iteration, as yet demonstrated by [27]. A proper formulation of a compressible projection algorithm, using a primitive variables formulation, considering non-isentropic effects in the conservation energy equation based on the pressure variable, has never been proposed, and would be a significant step forward for this class of solvers in particular for the study of heat transfer problems. Indeed, there are two major advantages to using a projection method based on a primitive variables formulation, as presented in this work, rather than solvers based on a conservative variables formulation. Firstly, the present primitive formulation guarantees that the pressure derived from the equation of state matches the pressure computed by the semi-implicit pressure correction algorithm at each time step. Secondly, the formulation of the energy equation as a pressure equation allows the heat conduction term to be treated with an implicit temporal scheme. On the other hand, the disadvantage of a primitive variables formulation is the poor conservation of total energy, which can be a problem when trying to describe supersonic flows. However, the focus of the present solver is restricted to subsonic flows and future developments will allow the treatment of phase changes induced by pressure or temperature variations in compressible flows at low Mach numbers. Note that the present algorithm is not positive preserving for the pressure, as the one proposed in [40], and it does not prevent for negative pressure values. However, metastable thermodynamical states involving negative pressure values can be observed in liquids, as in some cavitating flows. Such states can be modeled with suitable equations of state (EoS) for which positive temperatures are associated to negative pressures, as for instance the van der Waals EoS [21,13].

Another important point addressed in this paper concerns the equations of state (EoS). Previous studies were essentially based on ideal fluid EoS, such as Tait EoS for the liquid phase and perfect gas EoS for the gaseous phase. In the present work a cubic EoS will be considered. The solver benefits from such a generic EoS which allows the description of both gas and liquid phases.

The present work describes the development of a fully compressible numerical solver for two-phase flows based on a complete entropic (i.e. non-isentropic) formulation of the Navier-Stokes and energy conservation equations, accounting for capillary effects and making use of a generic equation of state for both phases. The numerical tests proposed in this paper will focus essentially on the van der Waals equation which is the simplest cubic EoS. However, the numerical framework proposed is general enough to handle any EoS, provided the sound speed can be computed in both phases. As a sharp representation of the interface and related jump conditions is performed, the definition of the density is still thermodynamically consistent with the EoS on each side of the interface. Consequently, the overall solver is free of nonphysical sound speed, that on another side can occur for solvers based on a diffuse interface representation, due to the spurious density smoothing, as remarked in [35].

The solver is derived from the one developed for Euler equations by [20] and integrated in the home made code, $\mathcal{DIVA}$. The innovative splitting of the equations proposed in [20], to correctly handle capillary effects, is edited and extended to the more complete system of equations which is considered here. As the proposed numerical solver is based on a primitive formulation of the conservation equations, its applicability field is restricted to subsonic two-phase flows, without any other assumptions on the Mach number while $Ma < 1$.

In the following, the mathematical formalism and the numerical algorithms are described. Then different validation test cases are described and analyzed in order to verify several important characteristics of the solver: acoustic waves propagation, thermal and density field interaction, heat conduction in single and two-phase flows, interface acoustic interaction and thermodynamic features.

2. Mathematical formalism

2.1. Primitive conservation laws

A two-phase compressible flow can be described with the following form of the conservation equations written in terms of the primitive variables, i.e. the density ρ and the velocity vector $\vec{u}$, for the mass and momentum conservation, respectively,

$$\frac{D\rho}{Dt} + \rho\nabla\cdot\vec{u} = 0, \tag{1}$$

$$\frac{D\vec{u}}{Dt} + \frac{\nabla p}{\rho} = \frac{1}{\rho}\nabla\cdot\boldsymbol{\tau} + \frac{\sigma\kappa\vec{n}\delta_\Gamma}{\rho} + \vec{g}, \tag{2}$$

where p is the pressure field, $\vec{g}$ is the gravity acceleration, and $\boldsymbol{\tau}$ the tensor of viscous constraints defined as,

$$\boldsymbol{\tau} = \mu(\nabla\vec{u} + \nabla\vec{u}^T) - \frac{2}{3}\mu\nabla\cdot\vec{u}\boldsymbol{I}, \tag{3}$$

which is valid for a compressible Newtonian fluid, with μ the dynamic viscosity and $\boldsymbol{I}$ the identity matrix. The variables σ, κ and $\vec{n}$ are related to interface properties and are named respectively the surface tension, the interface curvature and the normal vector pointing towards the liquid phase and δ_Γ is a δ-Dirac localized at the interface Γ. An additional equation will be added in the following to compute these variables. Moreover, unlike incompressible flows, such a system of equations is not complete if compressible flows are considered (since ρ is no longer a constant but a variable) and additional equations are required to close the system. In particular, as compressible flows involve a strong coupling between thermal and dynamical effects, the conservation energy equation has to be added to the overall system. It is usual to express this conservation law as an evolution equation for the internal energy e, such as,

$$\rho\frac{De}{Dt} = -p\nabla\cdot\vec{u} - \nabla\cdot\vec{q} + \boldsymbol{\tau}\otimes\nabla\vec{u}, \tag{4}$$

or an equation evolution for the enthalpy, $h = e + p/\rho$,

$$\rho\frac{Dh}{Dt} = \frac{Dp}{Dt} - \nabla\cdot\vec{q} + \boldsymbol{\tau}\otimes\nabla\vec{u}, \tag{5}$$

where $\vec{q}$ is the local heat flux defined, following the Fourier's law, as

$$\vec{q} = -k\nabla T, \tag{6}$$

with k the thermal conductivity and T the temperature. The last term of the conservation energy law is the thermal release due to the viscous friction in the fluid domain. Finally, as the pairs of unknown variables $(e,\ T)$ or $(h,\ T)$ emerge from the latter equations, two equations of state must be specified, respectively, for the internal energy or enthalpy, and for the temperature. For example, if one considers a thermally perfect gas, the following relations hold to define the internal energy or the enthalpy,

$$e(T) - e_0 = c_v(T - T_0), \qquad h(T) - h_0 = c_p(T - T_0), \tag{7}$$

and a further equation of state from which the pressure field can be deduced,

$$p = \rho RT, \tag{8}$$

where R is the gas constant ($R = \mathcal{R}/W$ with $\mathcal{R} = 8,314$ J/mol/K and W molecular weight of the species). This results in a complete framework for the description of gas dynamics. Such solvers based on the above equations have enabled important advances in the field of gas dynamics simulations to calculate both subsonic flows at intermediate Mach number ($0.1 \leq Ma < 1$) and supersonic flows at high Mach number ($Ma \geq 1$). One should specify here, that a conservative formulation of conservation laws have to be solved in the latter case to compute a correct shock wave speed. However, one of the drawbacks of these solvers is to perform poorly at low Mach number, in regards to both stability and accuracy. Indeed, the time step is limited by the acoustic wave propagation speed, if an explicit temporal integration has been chosen. This results in a large difference between the stability time step constraint and the physical characteristic time of the flow at low Mach number, and thus in an oversized number of temporal iterations. Moreover, accuracy issues have also been reported for that kind of solver for which it can be demonstrated that the error depends on $O\left(\frac{1}{Ma}\right)$, as detailed in [14], and thus increases if the Mach number decreases. Some preconditioning techniques, as the one proposed in [54] may be used to alleviate this, by introducing a modified artificial sound speed. However these issues become critical in the framework of compressible two-phase flows for which a very low Mach number is generally observed in the liquid phase due to its high sound speed. To prevent these issues, another type of compressible solvers, based on a pressure formulation of the energy conservation

equation, have been developed for two-phase flows in the last decade [20,24,18]. As shown in [24], such solvers have the nice property of preserving asymptotically the incompressible limit, since the pressure equation tends to the well-known pressure Poisson equation of the incompressible projection method, in the limit of an infinite sound speed. However, these solvers have never been rigorously generalized to flows for which entropic effects, such as heat conduction and viscous friction, have to be considered. We propose hereafter a compressible two-phase flows solver with a energy conservation equation based on an entropy/pressure formulation that will enable to account for these entropic effects.

To develop this formulation, we will adopt thermodynamic relations in order to express the above system in terms of ρ, $\vec{u}$ and p as primitive variables. The pressure being expressed with the density and entropy $p(\rho, s)$, its differential will be developed as,

$$dp = c^2 d\rho + \left(\frac{\partial p}{\partial s}\right)_\rho ds, \tag{9}$$

which allows to introduce explicitly the sound speed c defined from the following relation:

$$c^2 = \left(\frac{\partial p}{\partial \rho}\right)_s. \tag{10}$$

The Maxwell relation can be used in order to express the pressure derivative with respect to entropy,

$$\left(\frac{\partial p}{\partial s}\right)_\rho \left(\frac{\partial s}{\partial \rho}\right)_p \left(\frac{\partial \rho}{\partial p}\right)_s = -1, \quad \rightarrow \quad \left(\frac{\partial p}{\partial s}\right)_\rho = -\frac{c^2}{\left(\frac{\partial s}{\partial \rho}\right)_p}. \tag{11}$$

From the first principle of thermodynamic ($dh = Tds + dp/\rho$) the thermodynamic derivatives of the enthalpy h with respect to s and ρ are:

$$\left(\frac{\partial h}{\partial s}\right)_p = T, \qquad \left(\frac{\partial h}{\partial p}\right)_s = \frac{1}{\rho}. \tag{12}$$

Moreover the following equality holds,

$$\left(\frac{\partial h}{\partial \rho}\right)_p = \left(\frac{\partial h}{\partial T}\right)_p \left(\frac{\partial T}{\partial \rho}\right)_p, \quad \rightarrow \quad \left(\frac{\partial h}{\partial \rho}\right)_p = -\frac{c_p}{\rho\alpha}, \tag{13}$$

with α isobaric expansion coefficient (see Eq. (37)) and c_p the specific heat at constant pressure. Combining Eqs. (12) and (13) we obtain,

$$\left(\frac{\partial s}{\partial \rho}\right)_p = \left(\frac{\partial s}{\partial h}\right)_p \left(\frac{\partial h}{\partial \rho}\right)_p, \quad \rightarrow \quad \left(\frac{\partial s}{\partial \rho}\right)_p = -\frac{c_p}{T\rho\alpha}. \tag{14}$$

Eventually, combining Eqs. (14), (11) and Eq. (9) we can express the total derivative of the pressure with the following equation,

$$\frac{Dp}{Dt} = c^2 \frac{D\rho}{Dt} + \frac{\rho c^2 T\alpha}{c_p} \frac{Ds}{Dt}. \tag{15}$$

It is noteworthy that this equation is an expression of the conservation energy principle, based on the pressure/entropy variable, since the first law of thermodynamics has been used in Eq. (12) to derive this expression. Pointing out that the entropy material derivative can be expressed as,

$$\rho \frac{Ds}{Dt} = \frac{-\nabla \cdot \vec{q} + \boldsymbol{\tau} \otimes \nabla \vec{u}}{T}, \tag{16}$$

and the material derivative of ρ in Eq. (15) being expressed thanks to Eq. (1), we finally obtain the following form of the conservation energy equation, expressed in terms of pressure,

$$\frac{Dp}{Dt} + \rho c^2 \nabla \cdot \vec{u} = \frac{c^2 \alpha}{c_p} \left(\boldsymbol{\tau} \otimes \nabla \vec{u} - \nabla \cdot \vec{q}\right), \tag{17}$$

which in conjunction with Eq. (1) and (2) gives the following system of equations which is used as a basis in the present work,

$$\frac{\partial \rho}{\partial t} + \nabla \cdot (\rho \vec{u}) = 0, \tag{18}$$

$$\frac{\partial \vec{u}}{\partial t} + \vec{u} \cdot \nabla \vec{u} + \frac{\nabla p}{\rho} = \frac{1}{\rho} \nabla \cdot \boldsymbol{\tau} + \frac{\sigma \kappa \vec{n} \delta_\Gamma}{\rho} + \rho \vec{g}, \tag{19}$$

$$\frac{\partial p}{\partial t} + \vec{u} \cdot \nabla p + \rho c^2 \nabla \cdot \vec{u} = \frac{c^2 \alpha}{c_p} \left[\boldsymbol{\tau} \otimes \nabla \vec{u} - \nabla \cdot \vec{q} \right]. \tag{20}$$

In [52], the following equivalent expression of a pressure based energy conservation equation, has been proposed,

$$\frac{\partial p}{\partial t} + \vec{u} \cdot \nabla p + \rho c^2 \nabla \cdot \vec{u} = \frac{\alpha}{\rho c_v \beta} \left(\boldsymbol{\tau} \otimes \nabla \vec{u} - \nabla \cdot \vec{q} \right), \tag{21}$$

with $\beta = \frac{1}{\rho} \left(\frac{\partial \rho}{\partial p} \right)_T$.

However in the latter study, a fully explicit solver was used, which does not enable to alleviate the acoustical time step constraint.

2.2. Jump conditions across the interface

We now present the jump conditions that must be taken into account to maintain mass conservation, momentum conservation and energy conservation across the interface if two-phase flows are considered.

Capillary effects depend on σ, the surface tension and κ, the local interface curvature. They can be taken into account with the surface tension force term in the right hand side of the momentum equation Eq. (19) or as a jump condition when solving a Poisson or a Helmholtz equation for the pressure in the framework of incompressible solvers [25,29] or compressible solvers [20,24], respectively.

The system of equations (18)-(20) describes the flow in each phase and at the interface the following set of jump conditions must be verified,

$$\left[\vec{u} \right]_\Gamma = 0, \tag{22}$$

$$[p]_\Gamma = \sigma \kappa + 2 \left[\mu \frac{\partial u_n}{\partial n} \right]_\Gamma - \frac{2}{3} \left[\mu \nabla \cdot \vec{u} \right]_\Gamma, \tag{23}$$

$$\left[-k \nabla T \cdot \vec{n} \right]_\Gamma = 0. \tag{24}$$

In the above formalism, no mass transfer is considered between the phases: this means that no phase change is possible, nor diffusion between the phases. Furthermore, thermodynamic equilibrium and zero entropy production at the interface are assumed, which implies that the temperature is continuous across the interface ($[T]_\Gamma = 0$) [22].

2.3. Equation of state for the gas and liquid phases

An important feature of compressible flows is the coupling between mechanical effects and thermal effects that can be described through the resolution of Navier-Stokes equations with mass and energy conservation equations. However, an equation of state (EoS) is required in order to close the system. In particular, one can remark that the local heat flux computation requires the temperature field evaluation, which can be expressed as a function of the density and pressure $T(\rho, p)$ in Eq. (20), since both variables can be obtained by solving their corresponding evolution equations. Other relations are mandatory in order to compute the sound speed c (defined by Eq. (10)), the isobaric coefficient α and the specific heat at constant pressure c_p. These relations must be deduced from an EoS which should be able to describe both the gas and liquid states. The well-known perfect gas EoS, $p = \rho R T$, is appropriate to describe gaseous states at high temperature and low pressure in a wide range, but does not hold for liquid states. On the other hand, liquid states can be described using for instance the Tate EoS, that however is not valid for a gas. Among all existing EoS, a cubic EoS has the interest of being able to describe both a gas state and a liquid state with a generic expression. In this type of equations, the density obeys a cubic polynomial equation,

$$\rho^3 + a_1 \rho^2 + a_2 \rho + a_3 = 0, \tag{25}$$

where a_1, a_2 and a_3 are parameters depending on the pressure, the temperature, species characteristics and the specific cubic EoS. Among the well known cubic EoS are van der Waals, Peng-Robinson and Redlich-Soave-Kwong equations. In the present work, the van der Waals EoS has been used and therefore in the following specific expressions obtained with the van der Waals EoS will be given. However, the implementation presented in this paper is valid for any cubic EoS and can be easily extended to be used with Peng-Robinson or Redlich-Soave-Kwong equations that should enable a more accurate description of the liquid and gas states than the van der Waals equation, as pointed out in [41].

Eq. (25) can be rewritten in the following form, where the relation between p, ρ and T appears explicitly,

$$p = \frac{\rho RT}{1-\rho B} - \frac{\rho^2 A}{1+\rho UB+\rho^2 VB^2} \tag{26}$$

where U and V are integer constant values that depend on the selected EoS. It can be demonstrated that the parameters A and B are functions of the critical temperature T_c and critical pressure p_c and that they are selected in order to verify proper thermodynamic conditions. The values of the coefficients for the van der Waals EoS are,

$$U = V = 0 \qquad A = \frac{27}{64}\frac{R^2 T_c^2}{p_c}, \qquad B = \frac{RT_c}{8p_c}. \tag{27}$$

The corresponding a_i coefficients of Eq. (25) are,

$$a_1 = -\frac{1}{B}, \qquad a_2 = \frac{(PB+RT)}{AB}, \qquad a_3 = -\frac{p}{AB}. \tag{28}$$

Combining Eq. (27) and Eq. (26), the explicit expression of p as a function of ρ and T given by the van der Waals EoS is obtained,

$$p = \frac{\rho RT}{1-\rho B} - \rho^2 A. \tag{29}$$

Similarly, the expression of T as a function of p and ρ is,

$$T = \frac{(p+\rho^2 A)(1-\rho B)}{\rho R}. \tag{30}$$

In order to evaluate the density ρ for a given p and T the roots of the third order polynomial Eq. (25) have to be computed. Moreover, if saturation conditions are reached, further thermodynamic equilibrium conditions have to be applied in order to compute the vapor-liquid coexistence curve [31]. However, the present work only deals with phases of two distinct species, diffusion at the interface is neglected and the operative conditions are in the limit of zero Jacob numbers (Ja$\rightarrow$ 0), that is without phase change. For every test case that will be presented in this paper the thermodynamic conditions are chosen in order to have a liquid phase and a vapor phase far from the two phase region coexistence conditions. With these hypothesis, in each phase the density can be computed by solving Eq. (25) using for instance the Cardan method as demonstrated in Appendix A. The sound speed, which is mandatory to compute several terms in Eq. (20), can be computed remarking that,

$$c^2 = \left(\frac{\partial p}{\partial \rho}\right)_s = \left(\frac{\partial p}{\partial \rho}\right)_T + \frac{T}{\rho^2 C_v}\left(\frac{\partial p}{\partial T}\right)_\rho^2. \tag{31}$$

Other expressions can be found to compute the sound speed but the previous one is well suited for the van der Waals EoS. Indeed, from Eq. (29), the following thermodynamic derivatives can be easily computed,

$$\left(\frac{\partial p}{\partial \rho}\right)_T = \frac{RT}{1-\rho B}\left(1+\frac{B\rho}{1-\rho B}\right) - 2\rho A, \tag{32}$$

$$\left(\frac{\partial p}{\partial T}\right)_\rho = \frac{\rho R}{1-\rho B}. \tag{33}$$

Combining Eqs. (32) and (31) the following complete expression of the sound speed from the van der Wall EoS is obtained,

$$c = \left(\frac{RT}{(1-\rho B)^2}\left(1+\frac{R}{C_v}\right) - 2\rho A\right)^{1/2}. \tag{34}$$

The specific heat at constant volume c_v is related to the c_v^0 at low density, which only depends on the temperature, by the relation:

$$c_v - c_v^0 = \int_\rho^{\rho^0} \frac{T}{\rho^2}\left(\frac{\partial^2 p}{\partial T^2}\right)_\rho d\rho, \tag{35}$$

which, for a cubic EoS, gives $c_v = c_v^0$. Constant values for c_v^0 are considered in this work. To complete the thermodynamical system defined in Eq. (20), the Mayer relation can be used to compute the specific heat at constant pressure c_p,

$$c_p = c_v + \frac{T\alpha^2}{\rho\beta}, \tag{36}$$

where α and β are the isobaric and isothermal expansion coefficients,

$$\alpha = -\frac{1}{\rho}\left(\frac{\partial \rho}{\partial T}\right)_p, \qquad \beta = \frac{1}{\rho}\left(\frac{\partial \rho}{\partial p}\right)_T. \tag{37}$$

As the van der Waals EoS does not allow to define a simple expression $\rho(T, p)$, the following expressions are proposed to determine more easily the coefficients α and β,

$$\alpha = \frac{1}{\rho}\frac{\left(\frac{\partial p}{\partial T}\right)_\rho}{\left(\frac{\partial p}{\partial \rho}\right)_T}, \qquad \beta = \frac{1}{\rho\left(\frac{\partial p}{\partial \rho}\right)_T}. \tag{38}$$

3. Numerical solver

Most two-phase flows imply low-Mach number conditions, especially in the liquid phase. There is therefore significant interest in developing a solver for compressible two-phase flows for which the terms responsible for acoustic wave propagation are discretized with an implicit time scheme. An interesting property of the entropy-pressure based formulation, previously presented, is the possibility to handle separately the acoustics terms and the convection terms. This approach differs from more classical formulations of the conservation energy equation, based on internal energy or enthalpy, for which the eigenvalues of the Jacobian matrix must be computed to determine the characteristics variables of the hyperbolic system. As a result, an implicit temporal discretization of the acoustical waves will be simplified with the proposed approach since it will only result in a linear system to solve the pressure equation, whereas more classical approaches would require to solve a non-linear system coupling all the equations.

3.1. Single phase semi-implicit compressible solver

In this subsection an algorithm that can be used to describe any single-phase subsonic flow, is presented. The algorithm is suitable either for flows for which compressible effects or density variations can be significant or not, while maintaining an unconditionally stable temporal discretization related to acoustical waves propagation. The following elementary first order temporal discretization can be proposed for the whole system of equations,

$$\frac{\rho^{n+1}-\rho^n}{\Delta t} + \nabla\cdot(\rho\vec{u})^n = 0, \tag{39}$$

$$\frac{u^{n+1}-u^n}{\Delta t} + u^n\cdot\nabla\vec{u}^n = -\frac{\nabla p^{n+1}}{\rho^{n+1}} + \frac{1}{\rho^{n+1}}\nabla\cdot\boldsymbol{\tau}^n + \vec{g}, \tag{40}$$

$$\frac{p^{n+1}-p^n}{\Delta t} + u^n\cdot\nabla p^n + (\rho c^2)^n\nabla\cdot\vec{u}^{n+1} = \left(\frac{c^2\alpha}{c_p}\right)^n\left(\boldsymbol{\tau}^n\otimes\nabla\vec{u}^n - \nabla\cdot\vec{q}^n\right), \tag{41}$$

which is implicit for the acoustical terms. By carrying out the velocity splitting hereafter, which is classical in the framework of the projection method for the incompressible flow,

$$u^{n+1} = u^* - \Delta t\frac{\nabla p^{n+1}}{\rho^{n+1}}, \tag{42}$$

the following 4 steps algorithm can be obtained for the whole system.

First, solve the density field,

$$\rho^{n+1} = \rho^n - \Delta t\nabla\cdot(\rho\vec{u})^n. \tag{43}$$

Next, the intermediate velocity field u^* and the intermediate pressure p^* are updated,

$$u^* = u^n - \Delta t\left(u^n\cdot\nabla\vec{u}^n - \frac{1}{\rho^{n+1}}\nabla\cdot\boldsymbol{\tau}^n - \vec{g}\right), \tag{44}$$

$$p^* = p^n - \Delta t\vec{u}^n\cdot\nabla\vec{p}^n. \tag{45}$$

Then, by injecting Eq. (42) in Eq. (41), one obtains the following Helmholtz equation for the pressure field,

$$p^{n+1} - (\rho c^2)^n\Delta t^2\nabla\cdot\left(\frac{\nabla p^{n+1}}{\rho^{n+1}}\right) = p^* + \Delta t(\rho c^2)^n\nabla\cdot\vec{u}^* + \Delta t\left(\frac{c^2\alpha}{c_p}\right)^n\left(\boldsymbol{\tau}^n\otimes\nabla\vec{u}^n - \nabla\cdot\vec{q}^n\right), \tag{46}$$

which can be solved as a linear system for the pressure field and enables an implicit temporal discretization of the acoustical waves. It is noteworthy, that the resulting matrix is not symmetric definite positive. Indeed, one can verify that if a spatially

variable coefficient appears in front of the Laplacian, the matrix resulting from its spatial discretization is not symmetric. The matrix symmetry can be easily retrieved by dividing all the terms of the previous equation by $(\rho c^2)^n$. The following equation is obtained,

$$\frac{p^{n+1}}{(\rho c^2)^n} - \Delta t^2 \nabla \cdot \left(\frac{\nabla p^{n+1}}{\rho^{n+1}} \right) = \frac{p^*}{(\rho c^2)^n} + \Delta t \nabla \cdot \vec{u}^* + \Delta t \left(\frac{\alpha}{\rho c_p} \right)^n \left(\boldsymbol{\tau}^n \otimes \nabla \vec{u}^n - \nabla \cdot \vec{q}^n \right), \tag{47}$$

which results in a symmetric definite positive linear system, if a centered scheme is applied to discretize the Laplace operator. Finally, the velocity field accounting for pressure effects is updated with the following relation,

$$u^{n+1} = u^* - \Delta t \frac{\nabla p^{n+1}}{\rho^{n+1}}. \tag{48}$$

To understand the choice that has been made to consider $(\rho c^2)^n$ instead $(\rho c^2)^{n+1}$ in Eq. (47) it is useful to consider the following equality:

$$\frac{1}{\rho c^2} \frac{\partial p}{\partial t} = \frac{\partial \left(\frac{p}{\rho c^2} \right)}{\partial t} - p \frac{\partial \left(\frac{1}{\rho c^2} \right)}{\partial t}. \tag{49}$$

In order to verify the best choice to write the discretized form of the left hand side of Eq. (49), a first order discretization is operated over the right hand side:

$$\frac{1}{\Delta t} \left[\left(\frac{p}{\rho c^2} \right)^{n+1} - \left(\frac{p}{\rho c^2} \right)^n - p^{n+1} \left(\frac{1}{\rho c^2} \right)^{n+1} + p^{n+1} \left(\frac{1}{\rho c^2} \right)^n \right] = \frac{1}{\Delta t} \left(\frac{p^{n+1}}{(\rho c^2)^n} - \frac{p^n}{(\rho c^2)^n} \right), \tag{50}$$

where p^{n+1} is considered in the development of the second term. Similarly, if p^n is considered instead of p^{n+1} the following equality is obtained:

$$\frac{1}{\Delta t} \left[\left(\frac{p}{\rho c^2} \right)^{n+1} - \left(\frac{p}{\rho c^2} \right)^n - p^n \left(\frac{1}{\rho c^2} \right)^{n+1} + p^n \left(\frac{1}{\rho c^2} \right)^n \right] = \frac{1}{\Delta t} \left(\frac{p^{n+1}}{(\rho c^2)^{n+1}} - \frac{p^n}{(\rho c^2)^{n+1}} \right). \tag{51}$$

Therefore, Eqs. (50) and (51) demonstrate that considering $(\rho c^2)^n$ in Eq. (47) corresponds to consider p^{n+1} in the development of the second term in the right hand side of Eq. (49) instead of p^n. Moreover, this choice for the temporal index of $1/(\rho c^2)$ in Eq. (47) is consistent with the explicit nature of the terms multiplied by it in the right hand side, that is p^* and the non-isentropic terms. One interest of the overall formulation is to remove the time step constraint due to the acoustical wave propagation since an implicit temporal discretization of the acoustic term is performed. This can be justified by considering a one-dimensional linearized form of the pressure evolution equation Eq. (46) which is similar to an unsteady convection-diffusion equation with a source term f,

$$\frac{\partial p}{\partial t} + a \frac{\partial p}{\partial x} = D \frac{\partial^2 p}{\partial x^2} + f, \tag{52}$$

where the pseudo-diffusion coefficient $D = c^2 \Delta t$ depends on the sound speed and on the time step. Applying a fully explicit temporal scheme and a standard centered finite difference scheme, the following sufficient stability conditions can be stated, from von Neumann stability analysis, as detailed in [46],

$$\frac{2D\Delta t}{\Delta x^2} \leq 1, \qquad \frac{a^2 \Delta t^2}{\Delta x^2} \leq \frac{2D\Delta t}{\Delta x^2} \tag{53}$$

from which the following stability conditions can be deduced,

$$\Delta t \leq \frac{\Delta x}{\sqrt{2} c}, \qquad a \leq \sqrt{2} c, \tag{54}$$

which are valid if the Mach number $Ma = a/c \leq \sqrt{2}$, as stated by the second condition. To the authors knowledge, a more complete analysis involving higher Mach numbers is not available and is out of the scope of this paper that focuses only on subsonic flows. This simplified analysis shows that an explicit temporal integration of Eq. (46) would require a stability condition based on the acoustical time step, which is usual for standard explicit compressible solvers. On the other hand, if a first order implicit temporal scheme is applied to the diffusion term and a first order explicit temporal scheme to the convection term, as proposed in Eq. (46), it can be found that the stability condition is alleviated and becomes,

$$\Delta t \leq \frac{\Delta x}{a}. \tag{55}$$

This condition is much less stringent, especially in the low Mach number regime, than the time step Eq. (54) of the explicit counterpart. This justifies briefly why the acoustic time step does not need to be imposed to ensure stability in the computations carried out with the proposed solver. Another interesting property of this solver can be highlighted by remarking in Eq. (46) that in the limits of $c^2 \to \infty$, $\mu \to 0$, and $k \to 0$, the pressure equation tends to the pressure equation for incompressible flows in a classical projection method,

$$\nabla \cdot \left(\frac{\nabla p^{n+1}}{\rho^{n+1}} \right) = \frac{\nabla \cdot \vec{u}^*}{\Delta t}. \tag{56}$$

This means that, in the limits of low Mach number ($Ma \to 0$), high Reynolds number ($Re \gg 1$) and high Peclet Number ($Pe \gg 1$), the present numerical scheme will be asymptotically preserving relatively to the incompressible regime. The interest of such a nice property will be demonstrated in the results section by a direct comparison between a standard incompressible two-phase flows solver and the proposed compressible two-phase flows solver.

3.2. Implicit treatment of the thermal diffusion source term

In Eq. (47) the heat conduction is treated with an explicit temporal scheme and appears in the right hand side. The thermal field T^n is computed from the pressure p^n and the density ρ^n making use of the EoS Eq. (30). Another possibility is to treat the heat conduction term in an implicit way by considering ∇T^{n+1} instead of ∇T^n. Indeed we can express T^{n+1} as a function of ρ^{n+1} which is known from the continuity equation propagation Eq. (43), and p^{n+1} which is the unknown of Eq. (47) making use of the EoS Eq. (30):

$$T^{n+1} = \frac{1 - B\rho^{n+1}}{R\rho^{n+1}} p^{n+1} + \frac{A\rho^{n+1}}{R}(1 - B\rho^{n+1}), \tag{57}$$

which in the following will be written in a more compact way as:

$$T^{n+1} = C^{n+1} p^{n+1} + D^{n+1}, \tag{58}$$

where $C^{n+1} = (1 - B\rho^{n+1})/(R\rho^{n+1})$ and $D^{n+1} = A\rho^{n+1}(1 - B\rho^{n+1})/R$ are functions of ρ^{n+1} only.

By replacing Eq. (58) in Eq. (47) (considering Eq. (6)) one gets the following equation where the heat conduction term is treated with an implicit temporal scheme:

$$\frac{p^{n+1}}{(\rho c^2)^n} - \Delta t^2 \nabla \cdot \left(\frac{\nabla p^{n+1}}{\rho^{n+1}} \right) - \Delta t \left(\frac{\alpha}{\rho c_p} \right)^n \nabla \cdot k \nabla \left(C^{n+1} p^{n+1} \right) = RHS, \tag{59}$$

$$RHS = \frac{p^*}{(\rho c^2)^n} + \Delta t \nabla \cdot \vec{u}^* + \Delta t \left(\frac{\alpha}{\rho c_p} \right)^n \left(\boldsymbol{\tau}^n \otimes \nabla \vec{u}^n + \nabla \cdot k \nabla (D^{n+1}) \right). \tag{60}$$

Note that in Eq. (59) the thermal field does not appear explicitly anymore but through the two primitive variables ρ and p. The present approach is made possible by the proposed formulation of the algorithm based on a primitive variables formulation. Note that a linear relation between T and p in the EoS, as for Van der Waals and perfect gas EoS, is required in order to maintain a linear system for the pressure equation. Being able to treat the temperature field with an implicit scheme will have very beneficial consequences for future developments, including phase change problems which will be the subject of future works.

3.3. Operator split formulation for reducing surface tension driven parasitic currents

In this section, the algorithm for a two-phase flow is presented. As pointed out in [20], spurious currents may occur when adding directly the surface tension force as a jump on the pressure field when solving a Helmhotz-type equation, as Eq. (47). In order to numerically solve the system of Eqs. (18)-(20), while preventing from spurious velocities, a splitting of the primitive variables and of the momentum equation is introduced, following the idea yet developed in [20]. The idea is to isolate the effects of the capillary terms in one equation associated to an incompressible field, which is characterized by a soleinodal velocity field. Eventually, if the following split is operated on the primitive variables,

$$\rho = \rho_0 + \rho_{st}, \qquad \vec{u} = \vec{u}_0 + \vec{u}_{st}, \qquad p = p_0 + p_{st}, \tag{61}$$

where u_{st} is the solenoidal part of the velocity field, we have $\nabla . \vec{u}_{st} = 0$ and $\rho_{st} = const$. For simplicity we will set $\rho_{st} = 0$. The above splitting is inserted into the system of Eqs. (18)-(20) which is rewritten in Eqs. (62)-(65),

$$\frac{\partial \rho}{\partial t} + \nabla \cdot (\rho \vec{u}) = 0, \tag{62}$$

$$\frac{\partial \vec{u_0}}{\partial t} + \vec{u} \cdot \nabla \vec{u} + \frac{\nabla p_0}{\rho} = \frac{1}{\rho} \nabla \cdot \boldsymbol{\tau}, \tag{63}$$

$$\frac{\partial \vec{u_{st}}}{\partial t} + \frac{\nabla p_{st}}{\rho} = \frac{\sigma \kappa \vec{n} \delta_\Gamma}{\rho}, \tag{64}$$

$$\frac{\partial p_0}{\partial t} + \frac{\partial p_{st}}{\partial t} + \vec{u} \cdot \nabla p_0 + \vec{u} \cdot \nabla p_{st} + \rho c^2 \nabla \cdot \vec{u_0} = \frac{c^2 \alpha}{c_p} \left[\boldsymbol{\tau} \otimes \nabla \vec{u} - \nabla \cdot \vec{q} \right]. \tag{65}$$

The momentum equation Eq. (19) has been split into two equations: Eq. (64) which contains the capillary effects and the soleinodal part of the velocity field $\vec{u}_{st}$, and Eq. (63) which contains the non soleinodal part of the velocity field $\vec{u}_0$ and the viscous terms.

A level set function ϕ, defined as the signed distance from the interface ($\phi > 0$ in the liquid, $\phi < 0$ in the gas and $\phi = 0$ at the interface), is introduced to describe the movement of the interface [37] with the following convection equation,

$$\frac{\partial \phi}{\partial t} + \vec{u}_{int} \cdot \nabla \phi = 0, \tag{66}$$

where $\vec{u}_{int}$ is the interface velocity. A reinitialization algorithm, as proposed in [47], is used to ensure that the ϕ-function maintains the signed distance property at the interface, all along the computation. Both the normal vector $\vec{n}$ and the curvature κ can be evaluated from the level set function ϕ using Eqs. (67),

$$\vec{n} = \frac{\nabla \phi}{\|\nabla \phi\|}, \qquad \kappa = -\nabla \cdot \vec{n}. \tag{67}$$

3.4. Semi-implicit projection algorithm for two-phase flows

The system of Eqs. (62)-(65) with Eq. (66) is discretized on a Cartesian staggered grid and in this section the temporal numerical algorithm employed to locally solve it is reported step by step. We will indicate with the upper script n the time index, and Δt is the time step.

1. The level set function is updated,

$$\phi^{n+1} = \phi^n - \Delta t \, \vec{u}^n \cdot \nabla \phi^n. \tag{68}$$

2. The density field is updated,

$$\rho^{n+1} = \rho^n - \Delta t \, \nabla \cdot (\rho \vec{u})^n. \tag{69}$$

3. Since $\nabla . \vec{u}_{st} = 0$, a projection method is applied and p_{st} can be evaluated solving the linear system resulting from the discretization of the following Poisson equation,

$$\nabla \cdot \left(\frac{\nabla p_{st}}{\rho} \right)^{n+1} = \nabla \cdot \left(\frac{\sigma \kappa \vec{n} \delta_\Gamma}{\rho} \right)^{n+1}. \tag{70}$$

4. Predictions p^* and $\vec{u_0}^*$ are evaluated considering only the convection effects for the pressure p, and also the viscous and volumetric forces for the velocity,

$$p^* = p^n - \Delta t (\vec{u}^n \cdot \nabla p^n), \tag{71}$$

$$\vec{u_0}^* = \vec{u_0}^n - \Delta t [(\vec{u}^n \cdot \nabla \vec{u}^n) - \frac{1}{\rho^{n+1}} \nabla \cdot (\mu (\nabla \vec{u}^n + \nabla \vec{u}^{nT}) - \frac{2}{3} \mu \nabla \cdot \vec{u}_0^n \boldsymbol{I}) - \vec{g}]. \tag{72}$$

5. A projection method is also applied in order to calculate the rest of the pressure field p_0. Specifically using Eq. (63) and the u_0^* evaluated in the previous step we have,

$$u_0^{n+1} = u_0^* - \Delta t \left(\frac{\nabla p_0}{\rho} \right)^{n+1} \quad \rightarrow \quad \nabla \cdot u_0^{n+1} = \nabla \cdot u_0^* - \Delta t \nabla \cdot \left(\frac{\nabla p_0}{\rho} \right)^{n+1}. \tag{73}$$

Therefore, an Helmholtz equation for the pressure p_0 is found and p_0^{n+1} is the solution of the following linear system,

$$\frac{(p_0)^{n+1}}{(\rho c^2)^n} - \Delta t^2 \nabla \cdot \left(\frac{\nabla p_0}{\rho} \right)^{n+1} = \frac{p^* - p_{st}^{n+1}}{(\rho c^2)^n} - \Delta t \nabla \cdot \vec{u}_0^* + \Delta t \left(\frac{\alpha}{\rho c_p} \right)^n \left[\boldsymbol{\tau}^n \otimes \nabla \vec{u}^n - \nabla \cdot \vec{q}^n \right]. \tag{74}$$

6. Finally, the velocity field is corrected with the following step,

$$\vec{u}^{n+1} = \vec{u}_{st}^n + \vec{u}_0^* - \Delta t \left[\left(\frac{\nabla p_0}{\rho} \right)^{n+1} + \left(\frac{\nabla p_{st}}{\rho} \right)^{n+1} - \left(\frac{\sigma \kappa \vec{n} \delta_\Gamma}{\rho} \right)^{n+1} \right]. \tag{75}$$

A Ghost Fluid method is employed in order to handle the sharp jump across the interface [17,25,29,33,48]. Specifically, ghost fields are defined for ρ and p_{st}, and constant extrapolations are computed following the methodology described in [4]. For what concerns spatial discretization, staggered grids are used for the velocity fields relative to the centered grid for the other variables. Convective terms are evaluated with fifth order WENO Z schemes [5], other spatial derivatives are approximated with standard second order centered schemes. One interesting feature of the proposed algorithm is to be compatible with previous famous works in the community focusing on numerical solvers for two-phase incompressible flows. See for instance [33,25,48] for more details on spatial schemes to handle jump conditions across the interface. The linear systems (70) and (74) are solved with a Black-Box MultiGrid solver [15]. The temporal integration described previously is based on first order IMplicit-EXplicit (IMEX) Euler scheme. This can be used as an elementary step to build a second order or third order Runge Kutta scheme. However, if a standard explicit Runge-Kutta scheme is used, this will just improve stability, but not accuracy. Indeed, a specific IMEX Runge Kutta scheme would be required, as those proposed in [3,6], for achieving higher order of the temporal discretization. The development of such higher order temporal discretizations for the proposed compressible projection method will be the object of future works.

3.5. Temporal stability condition

The viscous and diffusion terms are computed explicitly. Eventually, the time step Δt is limited by classical stability conditions on convection, viscosity and surface tension, that is it has to respect the overall condition,

$$\frac{1}{\Delta t} = \frac{1}{\Delta t_{conv}} + \frac{1}{\Delta t_{\mu}} + \frac{1}{\Delta t_{\sigma}}, \tag{76}$$

where Δt_{μ}, Δt_{conv} and Δt_{σ} come from the classical stability conditions on viscosity, convection and surface tension respectively and are given by,

$$\Delta t_{conv} = \frac{\Delta x}{max\|\vec{u}\|}, \quad \Delta t_{\mu} = \frac{1}{2}\frac{\rho \Delta x^2}{\mu}, \quad \Delta t_{\sigma} = \frac{1}{2}\sqrt{\frac{max(\rho)\Delta x^3}{\sigma}}. \tag{77}$$

More details on the numerical methodologies implemented and validated in the $\mathcal{DIVA}$ code can be found in the following references: [20,49–51,29,32,45,36,56,55]. Several validations of the numerical methods with experimental results can also be found in the following references [12,11,28].

4. Test cases: validation and demonstration

Two single-phase test cases are carried out to verify two aspects: the correct propagation of acoustic waves and the ability of the solver to simulate compressible flows at low Mach numbers where thermal effects are of major importance, such as free convection problems. Secondly, two-phase flow tests are carried out to verify the correct treatment of interfaces with large deformations and the coupling between interface deformation and thermodynamic effects. Finally, a demonstration of the coupling between acoustic waves and interface deformation will be presented.

4.1. Acoustic pulse propagation

The aim of this test case is to verify the ability of the solver in properly describe acoustic waves propagation. We consider a non viscous and non conductive perfect gas: under these hypothesis the flow is isentropic. The domain is a one-dimensional line, of length $L = 1$ m with periodic boundary conditions. The base flow is at rest, $u_0 = 0$, the pressure is $p_0 = 1 \times 10^5$ Pa, the temperature is $T_0 = 300$ K which for air corresponds to a density of $\rho_0 = 1.117$ kg.m^{-3}. The base flow is initially perturbed by superimposing a p' field with a Gaussian shape,

$$p' = \Delta p_0 e^{-\frac{1}{2}\left(\frac{x}{\Sigma}\right)^2}, \tag{78}$$

with $\Sigma = 0.1$ m and $\Delta p_0 = 0.1 p_0$ for the present test case. Considering an acoustic wave traveling towards positive x, the associated velocity perturbation field is,

$$u' = \frac{p'}{\rho_0 c_0}, \tag{79}$$

where $c_0 = 347.12$ m.s^{-1} is the speed of sound corresponding to the base flow. Finally, the initial density field perturbation is imposed considering the isentropic relation,

$$\rho' = \frac{p'}{c_0^2}. \tag{80}$$

The initial solution is given by:

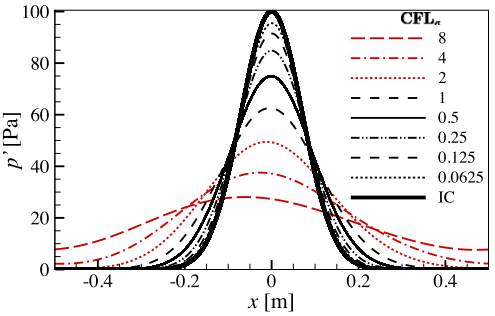

Fig. 1. Pressure perturbation field at the initial position (thick solid line, IC) and after one period, at $t = \tau$, for different time steps (based on a acoustic CFL$_a$).

$$p = p_0 + p', \qquad u = u', \qquad \rho = \rho_0 + \rho'. \tag{81}$$

The initial solution should theoretically be retrieved when the pulse, that should travel with a c_0 speed, has browsed a length L. The theoretical elapsed time is computed according to the following equation,

$$\tau = \frac{L}{c_0} \tag{82}$$

which gives $\tau = 0.046$ ms. The test case is performed with a first order temporal integration. First, a space convergence analysis is carried and the simulation is done using either 128, 256, 512 or 1024 cells. An acoustic Courant-Friedrichs-Lewy number, CFL_a, is introduced,

$$CFL_a = c_0 \frac{\Delta t}{\Delta x}, \tag{83}$$

where Δt and Δx are the time step and the mesh cell size respectively. The solver is implicit and no restriction associated with acoustic propagation is required in order to ensure stability, therefore the simulation can be carried out even with $CFL_a > 1$. However, in order to properly observe the acoustic propagation, we expect that the time step should be small enough. Therefore, a $CFL_a = 0.5$ is considered for the convergence analysis. Results at $t = \tau$ are shown in Fig. 1 for the 512 elements mesh, and compared with the initial condition (solid thick line) which is also the theoretical solution at $t = \tau$. Results for the other meshes are not reported because almost superimposed and differences between the curves are less than 0.0001%. This demonstrates the independence of the results with respect to the grid resolution for the present meshes. Therefore, all the other simulations are carried out with a 512 elements mesh. At $t = \tau$ the pulse retrieves the initial position, centered at $x = 0$, in agreement with the theory. This demonstrates that the solver correctly reproduces the acoustic wave propagation at the correct speed.

A parametric study is then carried out, varying the time step accordingly to a variation of CFL_a between 0.0625 and 8 and results at $t = \tau$ are shown in Fig. 1. The computation is stable even for the $CFL_a > 1$ thus demonstrating the expected stable behavior (see Section 3.1). The pulse retrieves its initial position at $t = \tau$ for $CFL_a < 1$, and for $CFL_a > 1$ a slight shift of the position is observed with respect to the theoretical solution thus indicating that the propagation speed is lower than the theoretical one. For every CFL_a, the amplitude of the pulse is lower than the theoretical one but numerical dissipation strongly increases for $CFL_a > 1$ and decreases when CFL_a decreases: the dissipation is 40% for $CFL_a = 1$ and 5% for $CFL_a = 0.0625$. As the order of convergence is around one, one could expect higher accuracy by introducing a higher order IMEX temporal scheme, as the one proposed in [3]. This will be the object of future works.

This test case validates the proposed solver for the simulation of acoustic waves propagation, and shows the necessity to use proper CFL_a if the objective is to follow the acoustic waves evolution, even if the computation remains stable also for $CFL_a \gg 1$.

4.2. Natural convection in a square

The objective of the present test case is to test the ability of the solver in reproducing a flow induced by a temperature gradient under the influence of the gravitational acceleration field. The test case of heat transfer by natural convection in an enclosure presented by Le Quéré et al. [43] is considered. The domain is a square 2D cavity of side L, filled will air initially at temperature T_0 and pressure p_0 (corresponding to a density ρ_0), and is shown in Fig. 2(a). Bottom and up walls are adiabatic, left and right walls are isotherm, at temperatures T_{wh} and T_{wc} respectively. The left wall is hotter than the right wall ($T_{wh} > T_0 > T_{wc}$), resulting in a horizontal temperature gradient. The gravity acceleration induces a upward movement of hot air and downward movement of cold air.

It can be demonstrated that the present test case is defined by a couple of parameters: the Rayleigh number Ra and the temperature ratio ϵ defined by the following equations,

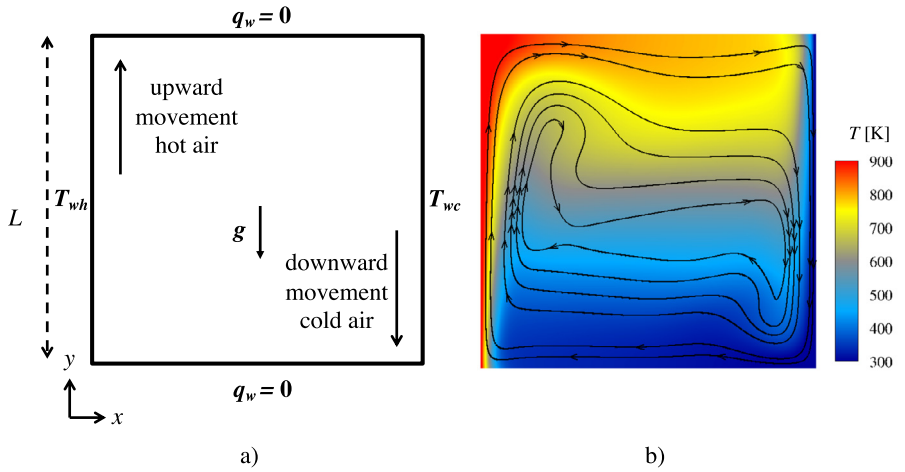

Fig. 2. Natural convection test case. a) Computational domain and boundary conditions. b) Temperature field and streamlines in stationary conditions ($t = 15$ s for the grid 512*512). (For interpretation of the colors in the figure(s), the reader is referred to the web version of this article.)

Table 1
Parameters for the natural convection test case *T1* from [43].

T_0 (K)	p_0 (Pa)	Ra	ϵ	T_{wh} (K)	T_{wc} (K)	Pr	μ (μPa.s)
600	101325	10^6	0.6	960	240	0.71	16.8

$$\mathrm{Ra} = \mathrm{Pr}\frac{g\rho_0^2(T_{wh} - T_{wc})L^3}{T_0\mu_0^2}, \qquad \epsilon = \frac{T_{wh} - T_{wc}}{T_{wh} + T_{wc}}, \tag{84}$$

where Pr is the Prandtl number and μ_0 the dynamic viscosity at T_0. We consider the test case with $\mathrm{Ra} = 10^6$, $\epsilon = 0.6$ and constant thermophysical properties (constant viscosity μ and thermal conductivity k), which is called *T1* in the work of Le Quéré et al. [43]. The ideal gas equation of state is used. The test case characteristics are summarized in Table 1. They correspond to a cavity of side $L = 0{,}0460307$ m.

Local and averaged Nusselt numbers, Nu and $\overline{\mathrm{Nu}}$, can be computed over the left and right walls:

$$\mathrm{Nu} = \frac{L}{k(T_{wh} - T_{wc})}k\frac{\partial T}{\partial x}, \qquad \overline{\mathrm{Nu}} = \frac{1}{L}\int_0^L \mathrm{Nu}(y)dy. \tag{85}$$

When the steady state regime is eventually reached, $\overline{\mathrm{Nu}}$ over the left and right walls become equal: $\overline{\mathrm{Nu}}_h = \overline{\mathrm{Nu}}_c$. The static pressure at steady state will be lower than the initial p_0 because of the mechanical energy involved in the movement in the cavity. The simulation is carried out with three different homogeneous grids, with 128×128, 256×256 and 512×512 elements. A snapshot of the temperature field superimposed with velocity iso-lines is shown in Fig. 2b) for the finer grid at t=15 s. We observe the stratification of the temperature field and the re-circulation of the fluid induced by the ascension of hot air and descent of cold air. Temporal evolutions of the average pressure and of the difference $\overline{\mathrm{Nu}}_h - \overline{\mathrm{Nu}}_c$ are shown for the free mesh resolutions in Fig. 3 over 15 seconds. A convergence of the results is observed and the finer grid results tend towards a stationary condition. In particular, after $t = 5$ s the temporal variation of the results is very slow and the difference between hot and cold Nu number is around 2.3×10^{-3} at $t = 15$ s. Quantitative results obtained with the finer grid are in agreement with the reference provided by [43] as reported in Table 2, with differences smaller than 0.02% for the ratio p/p_0 and 0.12% for $\overline{\mathrm{Nu}}_{c,h}$. The same simulations have been carried out considering an explicit or implicit treatment of the heat conduction term in the energy equation. Results are almost superimposed with small differences only in the transient phase ($t < 5$ s), smaller than 0.003% for the Nu numbers and 0.0005% for the pressure, and no differences in the stationary phase. Indeed the curves would appear as superimposed in Fig. 2 (where only the solutions obtained with an explicit heat conduction term are reported). This demonstrates the correct implementation of the numerical implicit scheme for the heat conduction term.

This section demonstrates that the semi-implicit compressible solver is well suited to handle free convection flows without any assumptions on the Mach number. Moreover, in such configurations, the acoustic time step has not to be imposed, since acoustic waves do not impact the flow.

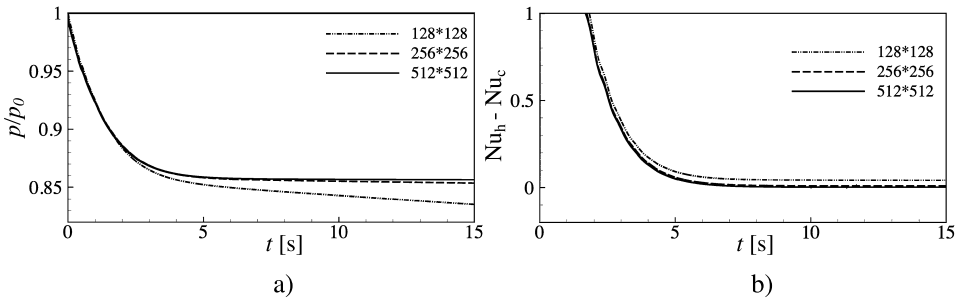

Fig. 3. Temporal evolution of the average pressure a) and the difference between cold and hot Nu numbers, b) for the three different grids.

Table 2
Natural convection test case results at $t = 15$ s: comparison between present numerical results with a grid (512×512), considering either an explicit or implicit treatment of the heat conduction term, and the reference values from [43].

	Reference	Present
$\overline{\mathrm{Nu}_h}$	8.85978	8.86885
$\overline{\mathrm{Nu}_c}$	8.85978	8.87113
p/p_0	0.856338	0.856515

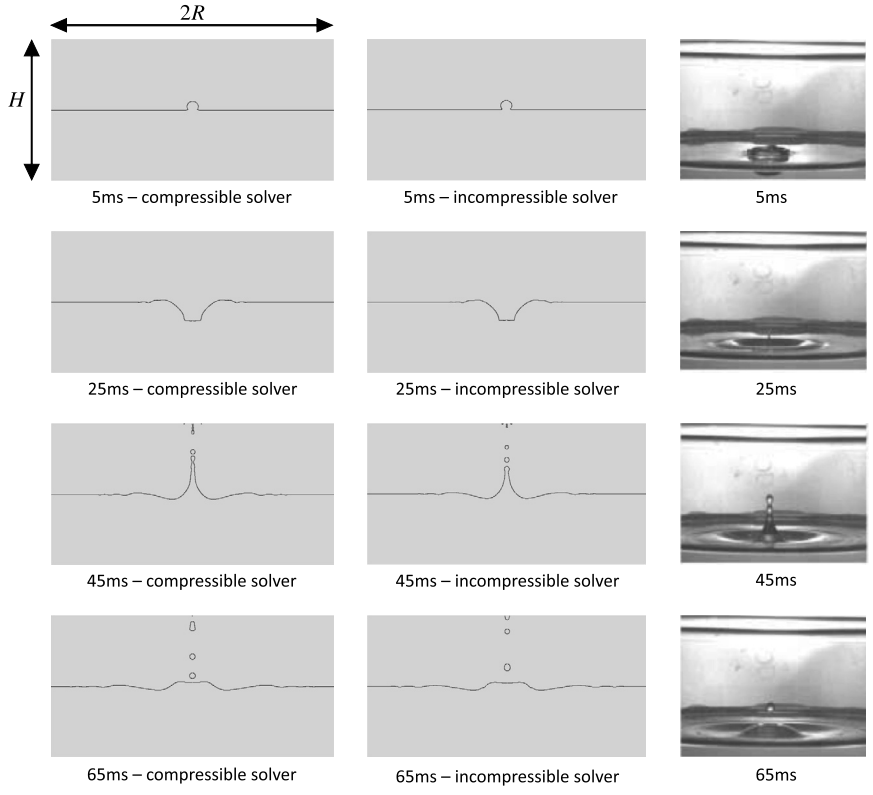

Fig. 4. Instantaneous snapshots of the interface obtained with compressible (left) and incompressible (middle) solvers and corresponding experimental (right) images from [34].

4.3. Falling drop over a liquid layer

The aim of the present test case is to verify the ability of the solver to simulate two phase flows, featuring strong interface deformations, at low Mach number. The falling of a liquid drop on a liquid layer is considered for this purpose and the experimental configuration of Manzello and Yang [34] is taken as a reference. The computational domain is a cylinder of height $H = 40$ mm and radius $R = 40$ mm (see Fig. 4). The bottom half of the domain is filled with water and the upper

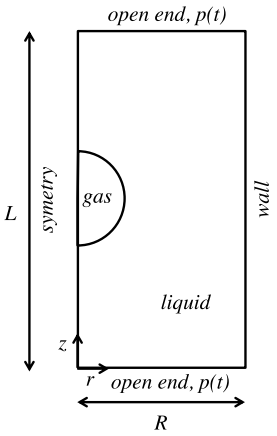

Fig. 5. Computational domain and boundary conditions for the test case of expansion of a bubble in an variable pressure environment.

half is filled with air (the interface is located at 20 mm from the bottom). The water density[1] is $\rho = 1000$ kg.m^{-3} and the dynamic viscosity is $\mu = 89$ µ.Pa. The surface tension is $\sigma = 0.072$ N.m^{-1}, corresponding to water in air at 293.15 K. A free boundary condition is imposed at the top of the domain to allow the fluid to leave and enter freely, while bottom and lateral walls are adiabatic. Two dimensional axisymmetric simulations are carried out with a homogeneous mesh of 1024×1024 elements. A drop of water is initially placed near the interface with a velocity of $v = 2.1908$ m/s, which corresponds to a Weber number $We = 123$ ($We = \rho v D/\sigma$), in order to reproduce the experimental conditions in terms of impact velocity [34]. The simulation is carried out both with the compressible solver and with the incompressible solver of the $\mathcal{DIVA}$ code. In terms of computational time, the simulation with the compressible solver takes twice as long as with the incompressible one. Indeed, for the compressible solver the number of steps involved in the algorithm is increased because of three main reasons: the Helmholtz-type equation for the pressure Eq. (47), the equation for the density field Eq. (69), and the equations to compute the extrapolations for the ghost fields defined for ρ and p_{st} (see section 3.4).

Numerical results obtained with the compressible solver are compared with the results obtained with the incompressible solver and the experimental data in Fig. 4 where temporal snapshots at 5, 25, 45 and 65 ms after the drop impact are shown.

At $t = 5$ ms, just after the drop impact, compressible and incompressible solvers give identical results that are in agreement with the experiment. At $t = 25$ ms, a crater is hollowing out and surface waves generated by the impact of the drop are observed both in numerical and experimental images. At $t = 45$ ms, a thick, high jet appears, from which droplets are detached. It seems that there is a time phase shift in the droplet detachments between the incompressible, compressible and experimental images and as a consequence the instantaneous number of droplets detached differs. However, these slight differences could be partly explained by the chaotic nature of the atomization process. At $t = 65$ ms, the jet has fallen and droplets are suspended both in the numerical and experimental cases, even thought the instantaneous observable droplets suspended is different (three in the numerical results and one in the experiments). Comprehensively, this comparison shows that the compressible and incompressible solvers provide results very close to the experiment and demonstrate the capability of the compressible solver in handling two phase flows with strong interface deformations in the low Mach number regime.

4.4. Expansion of a bubble in a variable pressure environment

The objective of this test case is to verify the correct implementation of the thermodynamic models available in the solver. In particular, the aim is to verify the coupling between density and pressure variations arising from the EoS. Two different EoS are available: the perfect gas equation, suitable for low pressure and high temperature gas, and the van der Waals, which is valid for both vapor and liquid phases over the entire domain of existence.

A bubble expansion in a liquid subjected to a variable pressure field is simulated. The simulation domain is shown in Fig. 5: it is a cylinder of height $L = 4$ mm and radius $R = 2$ mm, with two open ends and a lateral adiabatic wall. A bubble is initially placed at the center of the domain and the gravity acceleration field is artificially set to zero. The pressure in the domain is changed in time by applying a time varying Dirichlet condition for the pressure at the open ends borders, following the linear equation given by Eq. (86),

$$p = p_i - \frac{p_i - p_f}{t_f} \times t, \tag{86}$$

[1] The coefficients of the Van Der Waals EoS have been modified in order to obtain this value of ρ_l for $p = 1$ atm and $T = 293.15$ K. In fact, by default, the Van Der Waals EoS for water in these conditions would give $\rho_l = 494$ kg.m^{-3}.

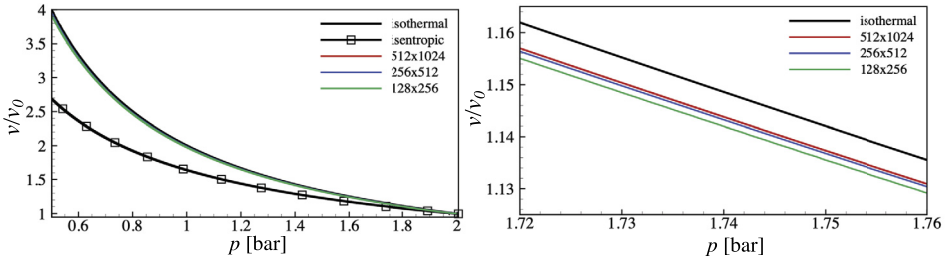

Fig. 6. Non-dimensional specific volume as a function of the average pressure in the bubble, obtained with a $t_f = 50$ ms, with 3 different grids, and comparison with the theoretical isentropic and isothermal transformations using a perfect gas EoS. Vapor: air. Liquid: water. a) Results over the entire pressure range. b) Closer view.

where p_i is the initial pressure, p_f the final pressure when $t = t_f$, t_f being the final time of the simulation. When the pressure decreases, the bubble volume should increase as a consequence of the density bubble decrease. By varying t_f and keeping the same initial and final pressure values, p_i and p_f, the pressure variation speed is modified. Small t_f will induce rapid bubble expansions and large t_f will induce slow bubble expansions. Analytically, the relation between the pressure and the bubble volume can be expressed using an isothermal or an isentropic transformation relation. A very slow expansion is expected to tend toward an isothermal transformation because a thermal equilibrium between the bubble and the surrounding liquid will have time to be established. On the other hand, fast bubble expansions are expected to follow an adiabatic transformation thus tending towards an isentropic transformation. Indeed, one can neglect the irreversibilities in such cases of fast expanding bubbles since the flow is almost irrotational and the expansion is faster than the characteristic time scale associated with thermal diffusion. Therefore, we expect a real expansion to evolve between the ideal isentropic and isothermal transformations. The objective of the present test case will be to verify this behavior for two different sub-cases:

- a low pressure case, for which the perfect gas EoS can be used to describe the vapor phase;
- a high pressure case, for which the perfect gas hypothesis does not hold and the van der Waals EoS is used for the vapor phase.

In both cases, the van der Waals equation is required to describe the liquid density, which is almost constant. In the first case, the density in the liquid will be around $\rho_l = 493.93$ kg.m^{-3} which is the solution of the van der Waals EoS for water at ambient pressure and temperature. In the second case the liquid density will be around $\rho_l = 200$ kg.m^{-3}, which is the solution of the van der Waals EoS for methane in a liquid state. It is noteworthy that more accurate solutions for liquid densities can be obtained by using more complex cubic EoS, as Peng-Robinson or Redlich-Soave-Kwong, for instance. This will be the subject of future investigations.

4.4.1. Expansion at low pressure: perfect gas EoS description

Isothermal and isentropic transformations for a perfect gas can be expressed with the relations given by Eqs. (87) and (88) between specific volume v and pressure p:

$$\text{isotherm}: \qquad v = \frac{p_i v_i}{p}, \tag{87}$$

$$\text{isentropic}: \qquad v = v_i \left(\frac{p_i}{p}\right)^{1/\gamma}, \tag{88}$$

where subscript i refers to initial values, and γ is the ratio between the specific heats. We are neglecting mass diffusion through the interface, therefore the bubble constitutes a closed system with a constant mass that is conserved in time. As a consequence, Eqs. (87) and (88) hold for the bubble volume. A bubble of air in liquid water is considered. Initial and final pressures are $p_i = 2$ bar and $p_f = 0.5$ bar, and the initial temperature is $T_i = 300$ K. In these conditions, a perfect gas EoS can be used to describe the vapor phase. A first simulation is carried out with $t_f = 50$ ms, using three different grids containing 128×256, 256×512 and 512×1024 elements. In this configuration the stability time step is constrained by viscous effects, and the time steps in the simulations are chosen accordingly. The bubble volume evolution versus the average pressure in the bubble is shown, for the three grids, in Fig. 6, where the isentropic and isothermal relations given by Eqs. (87) and (88) are also reported. Results obtained with the three grids are almost superimposed and behave as expected between the isothermal and isentropic transformations, though much closer to the isothermal for this t_f. The closer view in Fig. 6b) shows that the finer grid results tend towards the isothermal relation. These results show a grid convergence for the present setup, with differences for the bubble radius smaller than 9×10^{-3}%. For the following simulations, the coarse grid (128×256 elements) will be used.

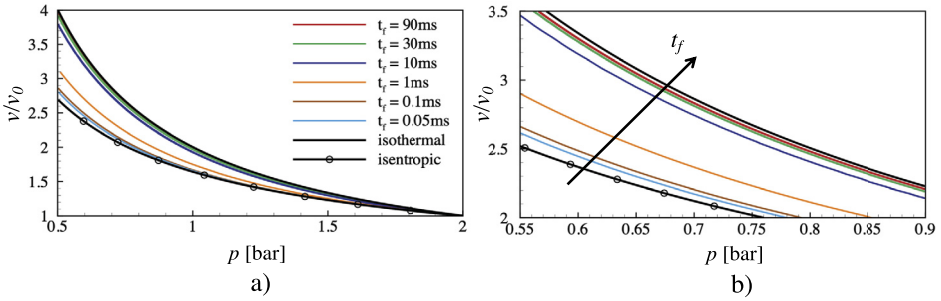

Fig. 7. Evolution of the bubble volume v as a function of the average pressure p for different speed of pressure temporal variation (higher t_f imply slower pressure variations).

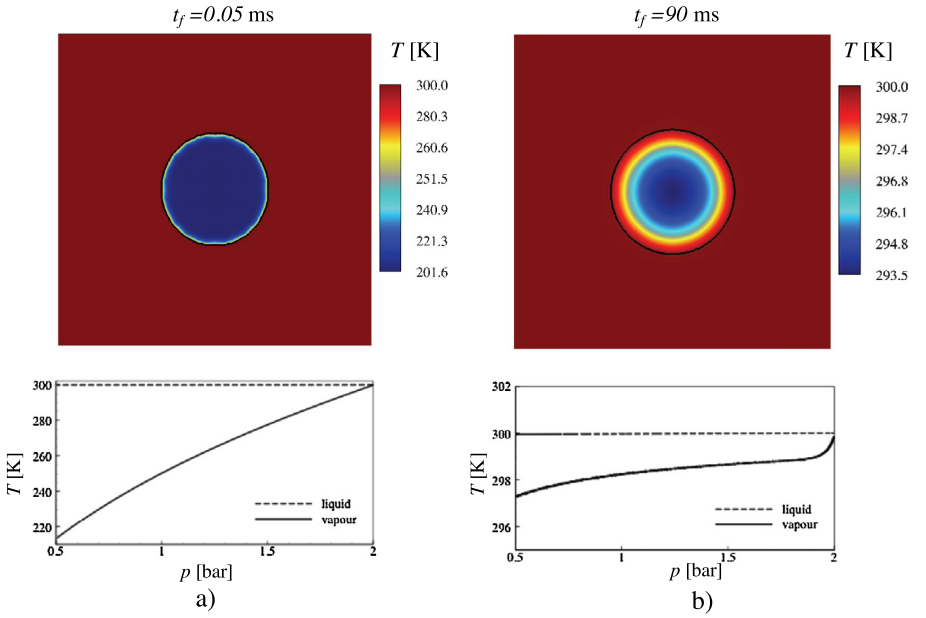

Fig. 8. Temperature fields reached at $t = t_f$ and corresponding average temperature for a) a rapid bubble expansion ($t_f = 5$ ms) and b) a slow bubble expansion ($t_f = 90$ ms).

A parametric study is carried out, varying t_f between 0.05 and 90 ms. Results are shown in Fig. 7a) over the entire pressure variation domain and a closer view is proposed in Fig. 7b). The bubble evolution tends toward the isothermal expansion for large t_f and the isentropic expansion for low t_f confirming the theoretical expectations.

The evolution of the average temperature in the vapor bubble and in the liquid is shown as a function of the average pressure in the vapor in Fig. 8a) for a rapid expansion ($t_f = 0.05$ ms) and Fig. 8b) for a slow expansion ($t_f = 90$ ms). The temperature field at the end of the simulation is also reported. For both cases the temperature in the liquid is almost constant and equal to $T_i = 300$ K. On the other hand, the behavior of the temperature in the vapor is very different. For the faster case, the temperature in the bubble undergoes a huge drop, a temperature around 200 K is reached in the center of the bubble center and a thin thermal boundary layer is formed around the bubble. The fast expansion of the bubble is quasi adiabatic thus inducing a huge cooling of the gas. On the contrary, the temperature in the bubble for the slow case is almost constant and only slightly decreases during the expansion. The final average temperature is 297 K and the minimum temperature is 293 K at the center of the bubble: the slow expansion of the bubble is quasi isothermal.

4.4.2. Expansion at high pressure: Van de Walls EoS

For a real gas, the perfect gas equation is no longer valid. Isothermal and isentropic transformations for a real gas can be expressed with the relations Eqs. (89) and (90) between v and p, derived using the van der Waals EoS Eq. (27):

$$\text{isotherm}: \quad pv^3 - v^2(pB + RT) + vA - AB = 0\,, \tag{89}$$

$$\text{isentropic}: \quad p = \frac{K^{(R/c_v)}}{(v-B)^{(1+c_v/R)}} - \frac{A}{v^2}\,, \tag{90}$$

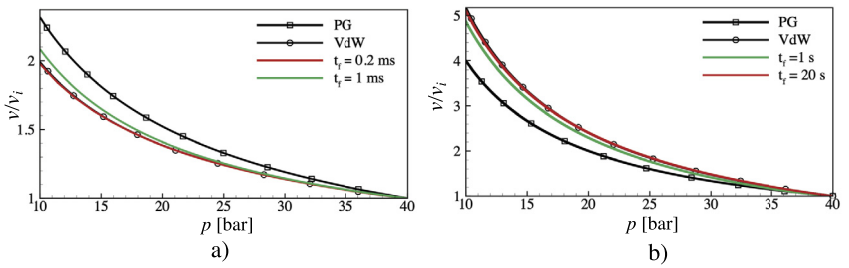

Fig. 9. Evolution of the specific volume as a function of the average pressure in the vapor for a bubble of nitrogen in liquid methane: numerical results (color curves) and theoretical evolution using a perfect gas or a Van der Waals EoS. a) Rapid bubble expansion that tends towards an isentropic transformation. b) Slow bubble expansion that tends toward the isothermal transformation.

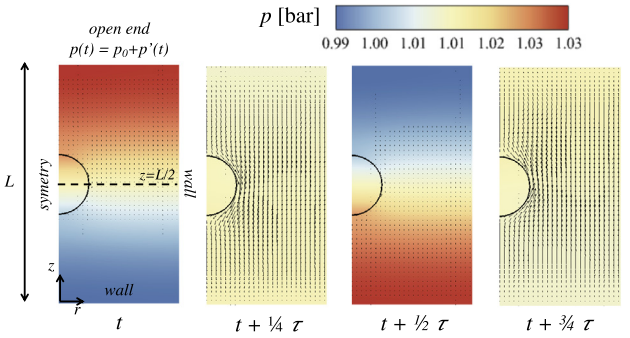

Fig. 10. Setup for the study of the drop shape evolution in an acoustic field. Evolution of the pressure and velocity fields over one temporal period for the pressure oscillation.

where c_v is the heat capacity at constant volume, R is the gas constant, A and B are given by Eq. (27) and K is a constant that can computed from v_i and p_i (see Appendix (27) for details on Eq. (90)). For the simulation in real gas regime, a nitrogen bubble in liquid methane at $T_i = 150$ K is considered and the pressure is varied from $p_i = 40$ bar to $p_f = 10$ bar. In these conditions real gas effects cannot be neglected and the van der Waals EoS is used to describe both the vapor and the liquid phases. Two different small t_f are considered in order to reproduce an adiabatic expansion: 0.2 and 1 ms. Results are shown in Fig. 9a), where both the real gas Eq. (90) and perfect gas Eq. (88) isentropic transformations are also reported for comparison. It appears that the two theoretical curves differ, as expected in the present high pressure conditions. The numerical results demonstrate that decreasing t_f, the bubble expansion tends towards the van der Waals EoS isentropic transformation, as it was expected. The same approach is developed for the isothermal expansion. Two different t_f are considered in order to reproduce an isothermal expansion, i.e. 1 and 20 s. Results are shown in Fig. 9b), where both the real gas (Eq. (90)) and perfect gas (Eq. (88)) isothermal transformations are also reported for comparison. When t_f increases, the bubble expansion tends toward the real gas isothermal transformation. In conclusion, the above results demonstrate the correct behavior of the thermodynamic models in the compressible solver and the ability to account for real gas effects.

4.5. Drop shape evolution in an acoustic field

In this test case the interaction between a droplet and an acoustic wave is computed with an asymmetric simulation in order to observe the deformation and potential breakup of the droplet induced by acoustic waves. The setup is shown in Fig. 10. The domain is a cylindrical cavity of height $L = 8$ mm filled with air at $T_0 = 300$ K and $p_0 = 101325$ Pa. A water droplet with an initial radius of $r = 1$ mm is positioned at the center of the domain ($r = z = 0$). The gravity acceleration is artificially set to zero. The bottom and lateral boundaries are adiabatic walls whereas the upper boundary is an open end and an acoustic oscillation boundary condition is imposed,

$$p(t) = p_0 + \Delta p \sin(\omega t), \tag{91}$$

with $\omega = 2\pi f_{1L}$ where $f_{1L} = c_0/L$ is the first acoustic mode frequency of the cavity, with $c_0 = 347$ m/s speed of sound in air at the present conditions. With the above conditions, the pressure wave frequency is $f_{1L} = 21695$ Hz. The pressure wave amplitude is set to 2% p_0 that is $\Delta p = 2026.5$ Pa. By imposing this boundary condition, a stationary acoustic wave is maintained in the domain. The setup is shown in Fig. 10, where the pressure and velocity fields evolutions over one oscillation period τ ($\tau = 1/f_{1L}$) are shown. The pressure wave propagates in time, both in the gas and in the liquid: the pressure in the drop is slightly greater than in the gas, by a difference corresponding to the surface tension (for the initial

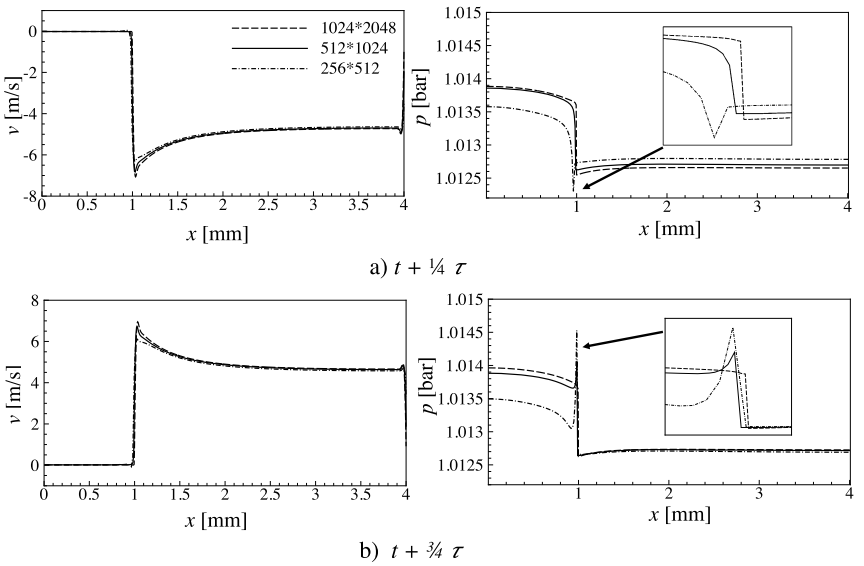

Fig. 11. Axial velocity evolution along the anti-nodal line ($z = L/2$) at two different times along one cycle corresponding to the maximum of velocity. Results are shown for different grid refinements.

circular drop the pressure jump across the interface is constant and equal to $\Delta p_{st} = 2\sigma/r = 116$ Pa). The pressure nodal line, which corresponds to the axial velocity anti-nodal line, is at the center of the domain (dashed line, $z = L/2$). As a consequence, during one period, the drop is subjected to an oscillating velocity field in the axial direction (z). The surface tension for the case shown in this figure is $\sigma = 0.058$ N.s. The maximum velocity at the nodal line, Δv, can be estimated considering an average impedance $\rho_0 c_0$ of the volume of air at T_0 and p_0,

$$\Delta v = \frac{\Delta p}{\rho_0 c_0}, \tag{92}$$

that results in a theoretical $\Delta v = 4.96$ m/s, which corresponds to a Weber number,

$$\mathrm{We} = \frac{\rho_0 \Delta v D}{\sigma}. \tag{93}$$

The axial velocity and pressure at $z = L/2$ are shown in Fig. 11 at two different instants along one cycle corresponding to the maximum and minimum of velocity oscillation (that is the second and fourth snapshots in Fig. 10). The first observation that can be made from Figs. 10 and 11 is that the pressure waves propagate both in the gas and inside the liquid drop but induce a velocity field which is much more important in the gas, in agreement with the higher impedance of the liquid ($(\rho_l c_l)/(\rho_v c_v) = 2500$ in the present case). The axial velocity far from the drop reaches maximum absolute values of 4.7 m/s, as shown in Fig. 11, in agreement with the theoretical expected value given by Eq. (92). The absolute velocity increases towards the drop interface: this is a consequence of the acceleration of the gas flow that goes around the drop. In the drop the axial velocity falls to almost a zero value. However, the tangential velocity is continuous across the interface and a very thin boundary layer is established. The pressure jump across the interface can be seen in Figs. 11a) and 11b): it has a value of 110 Pa in agreement with the theoretical value for the spherical drop at rest which is ($\Delta p_{st} = 2\sigma/r = 116$ Pa). The simulation has been carried out with several grid refinements in order to ensure a proper convergence analysis and results are reported in Fig. 11 for three uniform grids having a number of cells in the r and z direction of: 256×512, 512×1024 and 1024×2048 corresponding with cell sizes of 15 μm, 7.8 μm, and 3.9 μm, respectively. The axial velocity field is well captured with the three meshes and a convergence is observed. An over-shoot and an under-shoot on the pressure are observed with the coarser grids. These oscillations of the pressure at the interface are associated with the p_{st} field that contains the jump across the interface induced by the surface tension. If the mesh is not fine enough, the interface starts wrinkling since the beginning of the simulation, inducing oscillations on the p_{st} field at the interface, in particular in this region where the velocity variation at the interface is greater. This phenomenon disappears when increasing the mesh resolution and no oscillations are visible with the finest grid. This behavior is related to the well-known issue of parasitic currents induced by surface tension, which can be reduced by refining the grid.

The temporal evolution of the equivalent drop diameter is shown in Fig. 12a) for the different grids, over forty periods. The diameter decreases for the coarser grid and a liquid mass loss around 10% is reached at $t = 40\tau$. The mass loss reduces while increasing the grid resolution showing that the simulations converge towards a conservative solution. For the finest grid the mass loss is lower than 1% at $t = 40\tau$. Snapshots of the drop shape at $t = 40\tau$ are shown in Fig. 13 ($\mathrm{We} = 1$) and no significant difference is observed between the two finest grids. Considering the above observations, the 1024×2048 grid

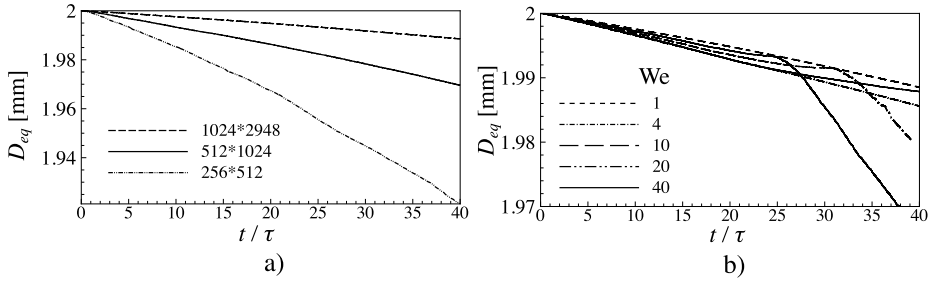

Fig. 12. Temporal evolution of the drop equivalent diameter. a) Comparison for different grid refinements for We = 1. b) Comparison for different We number cases, fine mesh 1024×2048.

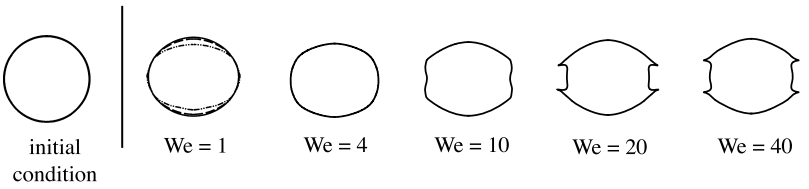

Fig. 13. Shape at $t = 40\tau$ of an initially spherical drop for different We numbers.

has be used to carry out the rest of the simulations for the present test case. Observing the drop shape at 40τ for We = 1 in Fig. 13, it appears that the drop shape, which initially is spherical, only slightly changes in time, in agreement with the low We number. In order to analyze the impact of the acoustic field on the interface deformation, a parametric study has been carried out increasing the We number up to 40. This has been achieved by decreasing the surface tension and keeping constant all the other parameters. The Ohnesorge number, $\mathrm{Oh} = \mu_l/(\rho_l * D * \sigma)^{1/2}$ is around Oh = 0.003. In these conditions, secondary atomization with a bag-breackup mode is expected for We > 11 [23]. We do not aim to go up to atomization in the present simulations and the axisymmetric hypothesis we make would not allow it. However, we can simulate the strong drop shape modification preceding the atomization. In terms of characteristic time, the characteristic time scale $t_c = D(\rho_l \rho_g)^{1/2}/v$ associated with atomization is around 8 ms in the present conditions, thus $t = 40\tau$ corresponds to $t = 0.22 t_c$. The equivalent diameter D_{eq} temporal evolutions over 40τ are shown in Fig. 12b) and the corresponding snapshots of the drop interface at 40τ are shown in Fig. 13). For We = 20 and We = 40 the D_{eq} shows a drop at 25 and 35τ respectively, while no particular drop in the diameter is observed for We $\leq$ 10. The diameter drop corresponds to a topological change in the drop shape as observed in Fig. 13. The acoustic velocity induces a deformation in the drop shape that flattens and eventually leads to the formation of two rims at an instant that corresponds with the diameter drop early observed.

These results demonstrate the ability of the present solver in describing the interaction between an acoustic field and a drop interface and open the door for further analysis including three dimensional simulations of secondary atomization induced by an acoustic field.

5. Conclusion

This paper presents an innovative numerical strategy for the study of two-phase compressible flows. The compressible solver proposed in this paper has many interesting features. It is able to describe acoustic waves, but it does not require to impose the stability constraint due to acoustic waves propagation. Indeed, imposing the latter stability constraint can be prohibitive in configurations with high density variations but for which sound propagation does not play any role, as for instance free convection or the expansion/compression of a bubble due to a pressure drop/increase. The proposed formulation gives a clear framework to account for heat conduction and viscous effects. It can be coupled to any equation of state, provided the sound speed can be computed. It works as well for liquids as for gases. It tends asymptotically to the incompressible projection method under usual assumptions of incompressible solvers, but it is also well suited to simulate low Mach number flows with density variations, as free-convection flows or a bubble growth. Its generalization to two-phase flows is quite straightforward. Even if an additional splitting on variables has to be carried out to impose the surface tension, general state-of-art and powerful techniques previously developed for incompressible two-phase flows can be applied directly to this two-phase compressible solver. Future works will tackle the generalization of this solver to higher order temporal discretization schemes, that could be based on IMEX Runge Kutta schemes. Coupling with extended physical models, as liquid-vapor phase change, supersonic flows, more complex equations of state and Immersed boundary methods, will be also investigated in the future.

CRediT authorship contribution statement

A. Urbano: Conceptualization, Investigation, Methodology, Software, Validation, Writing – original draft, Writing – review & editing. **M. Bibal:** Software, Validation, Writing – original draft, Writing – review & editing. **S. Tanguy:** Conceptualization, Investigation, Methodology, Software, Validation, Writing – original draft, Writing – review & editing.

Declaration of competing interest

The authors declare that they have no known competing financial interests or personal relationships that could have appeared to influence the work reported in this paper.

Acknowledgements

The authors gratefully acknowledge AID (Agence Innovation Défense) for funding the PhD thesis of Marie Bibal (N^o 2020213).

This work was granted access to the HPC resources of Curie/Occigen under the allocation A0072B10285 by GENCI in France.

This work was supported by the Chair for Advanced Space Concepts (SaCLab) resulting from the partnership between Airbus Defence and Space, Ariane Group and ISAE-SUPAERO.

Appendix A. Cardan algorithm applied to compute the density from the VdW EOS

In order to evaluate the density corresponding to a thermodynamic state defined by pressure p and temperature T, the roots of the Van der Waals EoS which is a cubic equation, have to be computed. The method of Cardan is employed. Let's consider the form of the Van der Waals EoS given by Eq. (25) with the coefficients of Eq. (28). A new variable $\tilde{\rho}$ is introduced and verifies,

$$\rho = \tilde{\rho} - \frac{a_1}{3} = \tilde{\rho} + \frac{1}{3B}\,. \tag{A.1}$$

Expressing Eq. (28) as a function of $\tilde{\rho}$ we obtain the following equation,

$$\tilde{\rho}^3 + \tilde{a}_1\tilde{\rho} + \tilde{a}_0 = 0\,, \tag{A.2}$$

where the coefficients $\tilde{a}_i$ are given by,

$$\tilde{a}_0 = -\frac{1}{27}\left(\frac{2}{B^2} - \frac{9p}{A} - \frac{9RT}{AB}\right) - \frac{p}{Ab}\,, \tag{A.3}$$

$$\tilde{a}_1 = -\frac{1}{3B^2} + \frac{p}{A} + \frac{RT}{AB}\,. \tag{A.4}$$

The cubic Eq. (A.2) has one, two or three real solutions depending on the sign of the discriminant $\Delta = -(4\tilde{a}_1^3 + 27\tilde{a}_0^2)$. Moreover, ρ must be positive. Crossing these requirements the following cases are possible,

- if $\Delta < 0$, one solution given by $\tilde{\rho}_1 = u + v$ where u and v are given by the following relations,

$$u = \left(\frac{-\tilde{a}_0 + \sqrt{\frac{-\Delta}{27}}}{2}\right)^{1/3}, \qquad v = \left(\frac{-\tilde{a}_0 - \sqrt{\frac{-\Delta}{27}}}{2}\right)^{1/3}; \tag{A.5}$$

- if $\Delta = 0$, two solutions given by,

$$\tilde{\rho}_1 = \frac{3\tilde{a}_0}{\tilde{a}_1}\,, \qquad \tilde{\rho}_2 = -\frac{3\tilde{a}_0}{2\tilde{a}_1}\,. \tag{A.6}$$

  If $\rho_1 > 0$ two solutions are available and it will be $\rho_v = \rho_1$ and $\rho_l = \rho_2$. If $\rho_1 < 0$ there is only one solution: $\rho = \rho_2$.
- if $\Delta > 0$, three solutions given by,

$$\tilde{\rho}_k = 2\sqrt{\frac{-\tilde{a}_1}{3}}\cos\left[\frac{1}{3}\cos^{-1}\left(\frac{-\tilde{a}_0}{2}\sqrt{\frac{-27}{\tilde{a}_1^3}}\right) + \frac{2k\pi}{3}\right], \quad k = 1, 2, 3 \tag{A.7}$$

  If $\rho_1 > 0$, there are two solutions, one for each phase: $\rho_v = \rho_1$ and $\rho_l = \rho_3$. If $\rho_1 < 0$ and $\rho_2 > 0$ then there are two solutions, one for each phase $\rho_v = \rho_2$ and $\rho_l = \rho_3$. If $\rho_1 < 0$ and $\rho_2 < 0$ there is a single phase solution: $\rho = \rho_3$.

Appendix B. Isentropic transformation for a real gas described by the Van Der Waals EOS

This appendix demonstrates how to obtain the isentropic relation expression Eq. (90) for a fluid described by the van der Waals EoS. Let's recall the first Clapyeron relation,

$$\delta Q = c_v dT + l dv, \tag{B.1}$$

where δQ is the heat absorbed during a reversible transformation, $v = 1/\rho$ is the specific volume and l is the isothermal dilation coefficient defined by,

$$l = T\left(\frac{\partial p}{\partial T}\right)_v. \tag{B.2}$$

The Clapyeron relation Eq. (B.1) can be combined with the first thermodynamic principle, $\delta e = \delta Q - pdv$, to express the internal energy variation,

$$de = c_v dT + (l - p)dv. \tag{B.3}$$

The expressions for p and T given by the van der Waals EoS Eq. (27) can be rewritten in terms of the specific volume v,

$$p + \frac{A}{v^2} = \frac{RT}{v - B}, \tag{B.4}$$

$$T = \frac{1}{R}\left(p + \frac{A}{v^2}\right)(v - B). \tag{B.5}$$

Using the van der Waals EoS the dilation coefficient l is given by,

$$l = p + \frac{A}{v^2}. \tag{B.6}$$

Replacing Eq. (B.6) in Eq. (B.3) gives,

$$de = c_v dT + \frac{A}{v^2}dv. \tag{B.7}$$

For an isentropic transformation $dS = 0$ which gives $de = -pdv$, and thus,

$$c_v dT + = -(p + \frac{A}{v^2})dv. \tag{B.8}$$

The right hand side of Eq. (B.8) is expressed using Eq. (B.4), thus obtaining the following relation between dT and dv along an isentropic transformation,

$$c_v dT = \frac{-RT}{v - B}dv, \tag{B.9}$$

which can be integrated between two states. Finally, the temperature T is replaced by its expression as a function of p and v, Eq. (B.5), thus yielding to the following relation between p and v along an isentropic transformation,

$$\left(p + \frac{A}{v^2}\right)^{\alpha}(v - B)^{\alpha+1} = K \qquad \text{with} \qquad \alpha = \frac{c_v}{R}, \tag{B.10}$$

where K is a constant. Eq. (B.10) can be used to relate p and v between two states along an isentropic transformation.

References

[1] M. Aanjaneya, S. Patkar, R. Fedkiw, A monolithic mass tracking formulation for bubbles in incompressible flow, J. Comput. Phys. 247 (2013) 17–61.
[2] M. Arienti, M. Sussman, A numerical study of the thermal transient in high-pressure diesel injection, Int. J. Multiph. Flow 88 (2017) 205–221.
[3] U.M. Ascher, S.J. Ruuth, R.J. Spiteri, Implicit-explicit Runge-Kutta methods for time-dependent partial differential equations, Appl. Numer. Math. 25 (1997) 151–167.
[4] T.D. Aslam, A partial differential equation approach to multidimensional extrapolation, J. Comput. Phys. 193 (2003) 349–355.
[5] R. Borges, M. Carmona, B. Costa, W. Don, An improved weighted essentially non-oscillatory scheme for hyperbolic conservation laws, J. Comput. Phys. 227 (2008) 3191–3211.
[6] S. Boscarino, J.-M. Qiu, G. Russo, T. Xiong, A high order semi-implicit IMEX WENO scheme for the all-Mach isentropic Euler system, J. Comput. Phys. 392 (2019) 594–618.
[7] R. Caiden, R.P. Fedkiw, C. Anderson, A numerical method for two-phase flow consisting of separate compressible and incompressible regions, J. Comput. Phys. 166 (2001) 1–27.
[8] J.-P. Caltagirone, S. Vincent, C. Caruyer, A multiphase compressible model for the simulation of multiphase flows, J. Comput. Phys. 50 (2011) 24–34.
[9] C. Chang, X. Deng, T.G. Theofanous, Direct numerical simulation of interfacial instabilities: a consistent, conservative, all-speed, sharp-interface method, J. Comput. Phys. 242 (2013) 946–990.

[10] S. Cho, G. Son, Numerical simulation of acoustic droplet vaporization near a wall, Int. Commun. Heat Mass Transf. 99 (2018) 7–17.
[11] A. Dalmon, M. Lepilliez, S. Tanguy, R. Alis, E.-R. Popescu, R. Roumiguié, T. Miquel, B. Busset, H. Bavestrello, J. Mignot, Comparison between the fluidics experiment and direct numerical simulations of fluid sloshing in spherical tanks under microgravity conditions, Microgravity Sci. Technol. 31 (1) (2019).
[12] A. Dalmon, M. Lepilliez, S. Tanguy, A. Pedrono, B. Busset, H. Bavestrello, J. Mignot, Direct numerical simulation of a bubble motion in a spherical tank under external forces and microgravity conditions, J. Fluid Mech. 849 (2018).
[13] K. Davitt, E. Rolley, F. Caupin, A. Arvengas, S. Balibar, Equation of state of water under negative pressure, J. Chem. Phys. 133 (2010) 174507.
[14] P. Degond, M. Tang, All speed scheme for the low Mach number limit of the isentropic Euler equations, Commun. Comput. Phys. 10 (2011) 1–31.
[15] J.E. Dendy, Black box multigrid, J. Comput. Phys. 48 (1982) 366–386.
[16] J.P.V. Doormaal, G.D. Raithby, Enhancements of the simple method for predicting incompressible fluid flows, Numer. Heat Transf. 7 (2) (1984) 147–163.
[17] R.P. Fedkiw, T. Aslam, B. Merriman, S. Osher, A non-oscillatory eulerian approach to interfaces in multimaterial flows (the ghost fluid method), J. Comput. Phys. 152 (1999) 475–492.
[18] D. Fuster, S. Popinet, An all-Mach method for the simulation of bubble dynamics problems in the presence of surface tension, J. Comput. Phys. 374 (2018) 752–768.
[19] M. Herrmann, A sharp interface in-cell-reconstruction method for volume tracking phase interfaces in compressible flows, in: Proceedings of the Summer Program, CTR, 2016.
[20] G. Huber, S. Tanguy, J.-C. Béra, B. Gilles, A time splitting projection scheme for compressible two-phase flows. Application to the interaction of bubbles with ultrasound waves, J. Comput. Phys. 302 (2015) 439–468.
[21] A.R. Imre, On the existence of negative pressure states, Phys. Status Solidi 244 (3) (2007) 893–899.
[22] M. Ishii, T. Hibiki, Thermo-Fluid Dynamics of Two-Phase Flow, 2 edition, Springer-Verlag, New York, 2011.
[23] M. Jain, R.S. Prakash, G. Tomar, R. Ravikrishna, Secondary breakup of a drop at moderate Weber numbers, Proc. R. Soc. Lond. A 471 (2014) 2014.
[24] M. Jemison, M. Sussman, M. Arienti, Compressible, multiphase semi-implicit method with moment of fluid interface representation, J. Comput. Phys. 279 (2014) 182–217.
[25] M. Kang, R.P. Fedkiw, X.-D. Liu, A boundary condition capturing method for multiphase incompressible flow, J. Sci. Comput. 15 (323–360) (2000).
[26] M. Kassemi, O. Kartuzova, S. Hylton, Validation of two-phase cfd models for propellant tank self-pressurization: crossing fluid types, scales, and gravity levels, Cryogenics 89 (2018) 1–15.
[27] N. Kwatra, J. Su, J.T. Grétarsson, R. Fedkiw, A method for avoiding the acoustic time step restriction in compressible flow, J. Comput. Phys. 228 (2009) 4146–4161.
[28] B. Lalanne, N.A. Chebel, J. Vejražka, S. Tanguy, O. Masbernat, F. Risso, Non-linear shape oscillations of rising drops and bubbles: experiments and simulations, Phys. Fluids 27 (2015).
[29] B. Lalanne, L.R. Villegas, S. Tanguy, F. Risso, On the computation of viscous terms for incompressible two-phase flows with level set/ghost fluid method, J. Comput. Phys. 301 (2015) 289–307.
[30] J. Lee, G. Son, A sharp-interface level-set method for compressible bubble growth with phase change, Int. Commun. Heat Mass Transf. 86 (2017) 1–11.
[31] J. Lekner, Parametric solution of the van der Waals liquid-vapor coexistence curve, Am. J. Phys. 50 (2) (1982) 161.
[32] M. Lepilliez, E.R. Popescu, F. Gibou, S. Tanguy, On two-phase flow solvers in irregular domains with contact line, J. Comput. Phys. 321 (2016) 1217–1251.
[33] X.-D. Liu, R.P. Fedkiw, M. Kang, A boundary condition capturing method for Poisson's equation on irregular domains, J. Comput. Phys. 160 (2000) 151–178.
[34] S.L. Manzello, J.C. Yang, An experimental study of a water droplet impinging on a liquid surface, Exp. Fluids 32 (2002) 580–589.
[35] O.L. Metayer, J. Massoni, R. Saurel, Elaborating equations of state of a liquid and its vapor for two-phase flow models, Int. J. Therm. Sci. 43 (2004) 265–276.
[36] A. Orazzo, S. Tanguy, Direct numerical simulations of droplet condensation, Int. J. Heat Mass Transf. 129 (2019) 432–448.
[37] S. Osher, J. Sethian, Fronts propagating with curvature-dependent speed: algorithms based on Hamilton–Jacobi formulations, J. Comput. Phys. 79 (1988) 12–49.
[38] S.V. Pantakar, Numerical Heat Transfer and Fluid Flow, Hemisphere Publishing Co., 1980.
[39] S.V. Pantakar, D.B. Spalding, A calculation procedure for heat, mass and momentum transfer in three-dimensional parabolic flows, Int. J. Heat Mass Transf. 15 (1972) 1787–1806.
[40] S. Patkar, M. Aanjaneya, W. Lu, M. Lentine, R. Fedkiw, Towards positivity preservation for monolithic two-way solid-fluid coupling, J. Comput. Phys. 312 (May 2016) 82–114.
[41] B.E. Poling, J.M. Prausnitz, J.P. O'Connell, The Properties of Gases and Liquids, 5th edition, McGraw-Hill, 2001.
[42] L. Qiu, W. Lu, R. Fedkiw, An adaptive discretization of compressible flow using a multitude of moving cartesian grids, J. Comput. Phys. 305 (2016) 75–110.
[43] P.L. Quéré, C. Weisman, H. Paillère, J. Vierendeels, E. Dick, R. Becker, M. Braack, J.B.B. Locke, Modelling of natural convection flows with large temperature differences: a benchmark problem for low Mach number solvers. Part 1. Reference solutions, Modél. Math. Anal. Numér. 39 (3) (2005) 609–616.
[44] R. Rajan, A. Pandit, Correlations to predict droplet size in ultrasonic atomisation, Ultrasonics 39 (2001) 235–255.
[45] L. Rueda-Villegas, R. Alis, M. Lepilliez, S. Tanguy, A ghost fluid/level set method for boiling flows and liquid evaporation: application to the Leidenfrost effect, J. Comput. Phys. 316 (2016) 789–813.
[46] E. Sousa, The controversial stability analysis, Appl. Math. Comput. 145 (2003) 777–794.
[47] M. Sussman, P. Smereka, S. Osher, A level set approach for computing solutions to incompressible two-phase flow, J. Comput. Phys. 114 (1994) 146–159.
[48] M. Sussman, K. Smith, M. Hussaini, M. Ohta, R. Zhi-Wei, A sharp interface method for incompressible two-phase flows, J. Comput. Phys. 221 (2007) 469–505.
[49] S. Tanguy, A. Berlemont, Application of a level set method for simulation of droplet collisions, Int. J. Multiph. Flow 31 (2005) 1015–1035.
[50] S. Tanguy, T. Ménard, A. Berlemont, A level set method for vaporizing two-phase flows, J. Comput. Phys. 221 (2007) 837–853.
[51] S. Tanguy, M. Sagan, B. Lalanne, F. Couderc, C. Colin, Benchmarks and numerical methods for the simulation of boiling flows, J. Comput. Phys. 264 (2014) 1–22.
[52] H. Terashima, M. Koshi, Approach for simulating gas-liquid-like flows under supercritical pressures using a high-order central scheme, J. Comput. Phys. 231 (2012) 6907–6923.
[53] H. Terashima, G. Tryggvason, A front-tracking/ghost-fluid method for fluid interfaces in compressible flows, J. Comput. Phys. 228 (2009) 4012–4037.
[54] E. Turkel, Preconditioned methods for solving the incompressible and low speed compressible equations, J. Comput. Phys. 72 (1987) 277–298.
[55] A. Urbano, S. Tanguy, C. Colin, Direct numerical simulation of nucleate boiling in zero gravity conditions, Int. J. Heat Mass Transf. 143 (2019) 118521.
[56] A. Urbano, S. Tanguy, G. Huber, C. Colin, Direct numerical simulation of nucleate boiling in micro-layer regime, Int. J. Heat Mass Transf. 123 (2018) 1128–1137.
[57] F. Xiao, R. Akoh, S. Ii, Unified formulation for compressible and incompressible flows by using multi-integrated moments ii: multi-dimensional version for compressible and incompressible flows, J. Comput. Phys. 213 (2006) 31–56.